

### **BACHELOR THESIS**

## Water Injection in Gas Turbines - Kinetic Modeling with Cantera

### **Author:**

Severin Maximilian Reiz

### **Matrikel-No:**

03633334

### **Supervisor:**

Prof. Dr.-Ing. Thomas Sattelmayer Stephan Lellek, M.Sc.

June 11, 2015

## Erklärung

Hiermit versichere ich, die vorliegende Arbeit anderen Quellen und Hilfsmittel als die angeg	selbstständig verfasst zu haben. Ich habe keine ebenen verwendet.
Ort, Datum	Severin Maximilian Reiz

## **Abstract**

Gas turbines play a significant role in the world's energy systems. As a special feature, they offer the capability to promptly adjust loads. With rising fluctuating energy sources gas turbines can be used to compensate gaps between energy supply and demand.

It is well known in literature that water injection in the combustion chamber can increase the gas turbines' performance; a possible feature to temporarily increase the energy production to desired loads.

A project at the Technical University of Munich investigates the impact of water injections in gas turbines' combustion chamber. For an experimental study an atmospheric test rig with a premix burner is used. The combustion uses natural gas as a fuel. Furthermore, the flame is aerodynamically stabilized using a swirler upstream. To establish gas turbine conditions the unburned mixture is additionally preheated to typical temperatures that occur in industrial setups. One part of the study concentrates on the influence of water injections on  $NO_x$  formation.

In this thesis a numerical kinetics simulation tool is developed and applied to predict  $NO_x$  emission values for water injected combustion. Flow information is analyzed using a 3D CFD calculation. A One-dimensional Free Flame models the kinetics until the mixture has reached 95% of the equilibrium temperature. Subsequently, a perfectly stirred chemical reactor calculates post flame phenomena using a probability density distribution of particles' residence times. For this study, the kinetics module *Cantera* is employed using the reaction mechanism *GRI3.0Mech* that is developed for hydrocarbon combustion.

Results are calculated for lean-premixed combustion with varying water injection proportions and preheat temperatures. On the one hand, a scenario of constant equivalence ratio for rising water injection rates is examined. On the other hand, a setup is studied where the flame temperature is kept constant.

A beneficiary effect of water injection on  $NO_x$  formation rates is found especially in the case of decreasing flame temperature. Furthermore, positive effects on  $NO_x$  emission values are also calculated in the setup of constant flame temperatures. The water influences the combustion chemistry by affecting radical concentrations.

In the end the predicted  $NO_x$  emissions are compared to experimental measurements. For the scenario of constant equilibrium ratios numerical calculations correlate closely to the experiment. For constant flame temperatures further investigations are required regarding the chemical influences.

# **Contents**

Li	st of	Figures			V
Li	st of	Tables			vii
No	omer	nclature		,	viii
1		roduction			1
	1.1 1.2	Motivation			1 1
2	The	eory			3
	2.1	Mathematical Modeling of Combustion Chemistry	 		3
		2.1.1 Reaction Kinetics	 		3
		2.1.2 Reaction Mechanisms	 		6
		2.1.3 Modeling of Laminar Premixed Flames	 		8
		2.1.4 Perfectly Stirred Reactor (PSR)	 		9
	2.2	Reaction Mechanisms of $NO_x$ formation	 		11
		2.2.1 Thermal/Zel'dovich Mechanism	 		11
		2.2.2 Prompt/Fenimore Mechanism	 		12
		2.2.3 Other Mechanisms	 		12
3	Met	thodology			14
	3.1	Description of the experimental setup	 		14
		3.1.1 Experimental test rig			14
		3.1.2 Flame stabilization methods	 		15
		3.1.3 Water injection	 		15
		3.1.4 Combustion chamber cooling and emission measurements	 		16
	3.2	One-dimensional Free Flame	 		17
		3.2.1 Measurement points	 		17
		3.2.2 Simulation Steps	 		18
		3.2.3 Post-processing	 		19
		3.2.4 Computation setup for series of measurements			19
	3.3	Chemical Reactor Modeling			
		3.3.1 Reactor Network constructed by Residence Times			

	Nor <b>Met</b>	B.2.1 Calculation of particle residence times in ANSYS  B.2.2 Generating a PDF of residence times in MATLAB  Reactor Network  B.3.1 Storage of Free Flame data at corresponding location  B.3.2 Reactor network calculations	5 5 5 5 5 5 5 6	6 7 7 8 8 8 9 9 0 0 0
	Met B.1 B.2 B.3	thodology steps Free Flame simulations B.1.1 Constant Equivalence Ratio B.1.2 Constant Flame Temperature Probability density distribution of residence times B.2.1 Calculation of particle residence times in ANSYS B.2.2 Generating a PDF of residence times in MATLAB Reactor Network B.3.1 Storage of Free Flame data at corresponding location B.3.2 Reactor network calculations Postprocessing of calculations	5 5 5 5 5 5 5 5 5 5 6 6	6 77788899900
	Met B.1 B.2 B.3	thodology steps Free Flame simulations B.1.1 Constant Equivalence Ratio B.1.2 Constant Flame Temperature Probability density distribution of residence times B.2.1 Calculation of particle residence times in ANSYS B.2.2 Generating a PDF of residence times in MATLAB Reactor Network B.3.1 Storage of Free Flame data at corresponding location B.3.2 Reactor network calculations	5 5 5 5 5 5 5 5 5 5 5 6	6 7 7 8 8 8 9 9 0
	Met B.1 B.2	thodology steps Free Flame simulations B.1.1 Constant Equivalence Ratio B.1.2 Constant Flame Temperature Probability density distribution of residence times B.2.1 Calculation of particle residence times in ANSYS B.2.2 Generating a PDF of residence times in MATLAB Reactor Network B.3.1 Storage of Free Flame data at corresponding location	5 5 5 5 5 5 5 5 5 5 5 5	6 7 7 8 8 8 9 9
	Met B.1 B.2	thodology steps Free Flame simulations B.1.1 Constant Equivalence Ratio B.1.2 Constant Flame Temperature Probability density distribution of residence times B.2.1 Calculation of particle residence times in ANSYS B.2.2 Generating a PDF of residence times in MATLAB Reactor Network	<b>5 5 5 5 5 5 5 5 5 5</b>	6 7 7 8 8 8 9 9
	Met B.1 B.2	thodology steps Free Flame simulations B.1.1 Constant Equivalence Ratio B.1.2 Constant Flame Temperature Probability density distribution of residence times B.2.1 Calculation of particle residence times in ANSYS B.2.2 Generating a PDF of residence times in MATLAB	<b>5 5 5 5 5 5 5 5 5 5</b>	6 7 7 8 8 8 9
	Met B.1	thodology steps Free Flame simulations B.1.1 Constant Equivalence Ratio B.1.2 Constant Flame Temperature Probability density distribution of residence times B.2.1 Calculation of particle residence times in ANSYS	5 5 5 5	6 7 7 8 8 8
	Met B.1	thodology steps Free Flame simulations B.1.1 Constant Equivalence Ratio B.1.2 Constant Flame Temperature Probability density distribution of residence times	<b>5</b> . 5 . 5 . 5 . 5	6 7 7 8 8
	Met B.1	thodology steps Free Flame simulations	<b>5</b> . 5 . 5 . 5	6 7 7 8
	Nor <b>Met</b>	thodology steps Free Flame simulations	5 5 5	6 <b>7</b> 7
	Nor <b>Met</b>	rmalization of Emission Concentrations	5 5	6 <b>7</b> 7
	Nor <b>Met</b>	rmalization of Emission Concentrations	. 5 <b>5</b>	6 <b>7</b>
	Nor	rmalization of Emission Concentrations	. 5	6
A				
A	Nor	rmalization of Emission Concentrations	5	6
Αŗ	pen	dix	5	5
5	Con	nclusion and Outlook	5	5
		4.5.2 Numerical adjustment with corresponding heat transfer	. 5	2
		4.5.1 Experimental Results		
	4.5	Comparison of Numerical Results with Experimental Data		
		4.4.2 Reaction path diagrams		
	1.1	4.4.1 Radical concentrations		
	4.4	• • • • • • • • • • • • • • • • • • • •		
		4.3.2 Discussion of developed reactor network approach		
	1.0	4.3.1 Discussion of simplifying assumptions		
	4.3	Limitations of developed reactor network		
		4.2.2 Pollutant formation of reactor network		
	7.2	4.2.1 Pollutant formation of One-dimensional Free Flame		
	4.2	Numerical Results - Constant Flame Temperature		
		4.1.2 Pollutant formation of reactor network		
	4.1	4.1.1 Pollutant formation in the One-dimensional Free Flame		
4	4.1	Numerical Results - Constant Equivalence Ratio		
4	Doo	sults and Discussion	2	=
	3.4			
		3.3.5 Heat loss of the combustion chamber		
		3.3.4 Computation setup for series of measurements	- 2	
		<ul><li>3.3.2 Particle Residence Time Calculation by CFD data</li></ul>	. 2	

# **List of Figures**

2.1	Schematic of a constant pressure, constant mass reactor	10
3.1	Experimental test rig [14]	14
3.2	Schematic of the burner - Recirculation zones in the combustion chamber $[19]$ .	15
3.3	Schematic of developed Reactor Network	21
3.4	Flame front approximation	
	Isosurface in ANSYS	22
3.5	Trajectories of particles after crossing the isosurface	22
3.6	Probability distribution of particles' residence times in the combustor after "cross-	
	ing" the flame- the polynomial fit in red, Histogram in blue	23
4.1	Sample temperature profile for different equivalence ratios, $\Omega = 0$ , $T_{pre} = 573 K$ .	26
4.2	Flame Temperatures for various water injection rates and preheat temperatures .	27
4.3	Typical profile for temperature and Nitrogen oxides, $T_{pre} = 573K$ , $\Phi = 0.625$	28
4.4	Exhaust $NO_x$ concentrations relative to corresponding dry unburnt configuration	29
4.5	Relative $NO_x$ emission values compared to flame temperature, $T_{pre} = 573K$	30
4.6	Typical profile for Nitrogen oxides concentration in a reactor, $T_{pre} = 573 K$ , $\Omega = 0$	31
4.7	Exhaust $NO_x$ concentrations calculated by the reactor network	32
4.8	Typical profile for radical concentrations over distance, $T_{pre} = 573K$ , $\Phi = 0.63$ .	34
4.9	Typical profile for Nitrogen oxides concentration over distance in a Free Flame,	
	$T_{pre} = 573 K, \Phi = 0.63 \dots$	35
4.10	Free flame $NO_x$ exhaust concentrations relative to dry configuration- constant	
	flame temperature	36
4.11	$NO_x$ emission concentrations predicted by reactor network at constant temper-	
	ature	37
	Typical profile for atomic oxygen concentrations, $T_{pre} = 673K$ , $\Omega = 0 \dots \dots$	42
4.13	Peak atomic Oxygen O concentrations and flame temperature - constant equiv-	
	alence ratio, $T_{pre} = 573K$	43
	Typical profile for $CH$ and $CH_2$ concentrations, $T_{pre} = 673K, \Phi = 0.71 \dots$	43
4.15	Peak atomic Oxygen O concentrations and $NO_x$ concentrations at constant tem-	
	perature	44
	Reaction Path diagrams at different Flame regions	46
		47
4.18	Reaction paths at 50% temperature progress at constant flame temperature, $T_{pre} =$	
	$573K, \Phi = 0.625$	48

4.19	Reaction Path diagrams of the post-flame zone for increasing water injections at	
	constant flame temperature, $T_{pre} = 673$ , $\Phi = 0.71$	49
4.20	Reaction Path diagrams for increasing water injections - setup of constant tem-	
	peratures, $T_{pre} = 473$ ,	50
4.21	Comparison of experimental and numerical $NO_x$ emission values at constant	
	equivalence ratio $\Phi$	51
4.22	Comparison of experimental and numerical $NO_x$ emission values at constant	
	flame temperature $T_{flame}$	52
4.23	Comparison absolute $NO_x$ emissions between experiment and simulation in-	
	cluding heat loss, $T_{pre} = 673$	53
	·	

# **List of Tables**

3.1	Species compositions of air and fuel used for all simulations	17
3.2	Summary of test conditions for series of measurements	18
3.3	Schematic of different .csv files for 95 % Free Flame data	23
A.1	Explanation of variables for normalization procedure	56
B.1	Setting of the particle injection region	58
B.2	Settings of injected particles	59

# Nomenclature

### **Greek characters**

$\dot{\omega}_k$	Reaction Rate producing species k	$mol \ s^{-1}$
$\dot{\omega}_T$	Heat release rate	W
λ	Thermal conductivity	$W m^{-1} K^{-1}$
ν	Stoichiometric Coefficient	_
Ω	Water-to-fuel ratio	
Φ	Equivalence Ratio	
$\Psi_j$	Progress Rate of reaction j	$mol\ s^{-1}$
ρ	Density	$kg m^{-3}$
Roma	an Characters	
$[S_k]$	Concentration of species k	$mol \ m^{-3}$
A	Arrhenius factor(unit depends on reaction order)	$m^3 mol^{-1} s^{-1}$
b	Empirical Arrhenius temperature exponent	
c	Concentration	$mol \ m^{-3}$
$C_p$	Heat capacity at constant pressure	$J kg^{-1}K^{-1}$
D	Proportional Diffusion Coefficient	$m s^{-1}$
$E_A$	Activation energy	$Jmol^{-1}$
$h_k$	Specific enthalpy of species k	$J kg^{-1}$
k	Reaction rate coefficient(unit depends on reaction order)	$m^3 mol^{-1} s^{-1}$
$K_c$	Equilibrium Constant	
M	Molar Mass	$k\sigma mol^{-1}$

m	Mass	kg
R	Universal Gas Constant	$Jmol^{-1}K^{-1}$
$s_L$	Laminar flame speed	$m s^{-1}$
и	Velocity	$m s^{-1}$
V	Volume	$m^3$
$V_k$	Correction Velocity of species k	m s
$W_k$	Molecular weight of species k	_
$Y_k$	Mass Fraction of species k	_
Ċ	Heat flux	W
Т	Temperature	K

## 1 Introduction

This work evolves from studies at a combustion chamber test rig at the Institute of Thermodynamics, Technical University of Munich, investigating the impact of Water Injection in Gas Turbine Combustion Chamber.

### 1.1 Motivation

Around the world countries face the transition to a more sustainable and renewable energy system. Wind and solar fluctuations however lead to a very non-uniform power production rate. Thus, there is a need for a more flexible energy grid that compensates temporary gaps between power demand and supply. One possible solution is a complementary energy source that can be adjusted to required loads.

Gas turbines are well suited as they offer the opportunity to instantly establish required power outputs. Additionally, they can be built anywhere and reach efficiencies up to 60%. Hence, gas turbines already play a major role in energy systems [10, 15, 23].

It is well known in literature that water injections in gas turbines increases the performance. A research project at the Technical University of Munich investigates this method. Its goal is to increase the power output whilst keeping the  $NO_x$  pollutant emissions constant.

Due to environmental reasons resulting pollutant formation has been a main field of interest in research. In a combustion with air however, Nitrogen oxides  $(NO_x)$  in the exhaust gas are not completely avoidable. Nitrogen oxides harm the environment by being responsible for the ozone depletion in the stratosphere, contribute to the greenhouse effect in the troposphere and are suspected of causing lung cancer. [9, 17, 24]

On the one hand water injections influence the  $NO_x$  formation physically by lowering the flame temperature. On the other hand the combustion chemistry is affected by changes in radical concentrations.

In order to predict  $NO_x$  emissions accurately and to investigate the combustion chemistry a numerical simulation is useful for various applications.

### 1.2 Objectives

The scope of this thesis is an investigation of  $NO_x$  formation using a numerical simulation in a premix swirl burner with water injection in the combustion chamber.

The flame in the investigated burner is stabilized through a recirculation zone induced by a conical swirler upstream along which the flame is formed (well described by Sangl and Mayer [18]).

First, principles of pollutant formation and mathematical modeling of flames are introduced. Thereafter, the basic methodology of the developed numerical simulation is described. As suggested by Fichet et al. [7] Computational Fluid Dynamics (CFD) of the burner is coupled with detailed reaction chemistry to predict minor species such as  $NO_x$ . [7]

Secondly, One-dimensional Free Flame simulations are conducted for different 'water to fuel' and 'fuel to air' ratios. Furthermore, the inlet temperature of the mixture is varied. The computations use the *Cantera 2.1.1* module with the detailed reaction mechanism *GRI-Mech 3.0. Cantera* is a software tool that solves problems involving diffusion, thermodynamics and chemical kinetics. The *GRI-Mech* is a detailed reaction mechanism for hydrocarbon combustion.

On the one hand, simulations for constant equivalence ratios with water injections are studied. On the other hand, a setup with constant flame temperatures while adding water is investigated. In order to identify reasons for changes in the combustion chemistry reaction path analyses are performed.

Subsequently, a reactor network is developed to numerically predict concentrations for the burner geometry in the test rig. Computational Fluid Dynamics (CFD) data has been employed to construct a probability density function (PDF) of particles' residence times. The different times are then represented by Perfectly Stirred Reactors (PSR) imposed with data from preceding Free Flame simulations.

## 2 Theory

In this chapter background knowledge on reaction chemistry and pollutant formation is explained.

### 2.1 Mathematical Modeling of Combustion Chemistry

Flame phenomena occur in many different setups. Two main classes exist in order to distinguish its characteristics: Premixed and Diffusion Flames.

Premixed Flames assume a perfectly mixed solution prior to the flame. This flame type appears most likely in the combustion of gases. In diffusion-type flames the mixing (mass diffusion) of fuel and oxidizer takes place during the combustion reaction. Fuel and oxidizer may be of different phase, e.g. in coal combustion. In general, the latter procedure favors process safety because flame propagation upstream is impossible, whereas the premixed case involves a cleaner combustion. Of course, also partially premixed flames exist that combine features of the two cases.

Additionally, the flow type significantly influences the flame behavior. Therefore one differentiates between the laminar and the turbulent case. Higher flame speeds and more power output can be achieved through the turbulent setup [20, 24].

With the growing availability of computing power many numerical flame simulation tools have been developed for research as well as industry fields. However, running simulations without a deep understanding of combustion theory will lead to many troubles [16]. In the following section underlying principles of mathematical models for flame simulations are explained.

### 2.1.1 Reaction Kinetics

In a reacting flame several processes such as chemical reaction, heat-/ mass-diffusion and flow phenomena occur simultaneously. The reaction itself is not infinitely fast but the mixture reacts within a time scale that is in the range similar to the diffusion and flow processes. These mechanisms interact with each other accordingly. As a matter of fact, reaction occurrence strongly depends on temperature, concentrations and on flow characteristics. A recirculation zone influences the flame by affecting mass diffusion processes.  $NO_x$  formation mechanisms often do not reach chemical equilibrium. Ergo, a description of reaction kinetics is essential for a reasonable numerical simulation of pollutant formation [24].

#### General Overview of Rate Laws and Reaction Orders

The rate law describes how fast a reaction is occurring. Given the general equation

$$A + B + C + \dots \xrightarrow{k} D + E + F + \dots$$
 (2.1)

where capital letters represent species one can formulate the reaction rate for example for species A, analogous for others, to be

$$\frac{d[A]}{dt} = -k * [A]^a * [B]^b * [C]^c \dots$$
 (2.2)

where lower-case letters (i.e. exponents) represent *individual reaction orders*. Since reaction 2.1 can involve intermediate steps, these individual reaction orders cannot be determined theoretically. Exponents are thus obtained using empirical data of reaction rates and hence are fitted decimal numbers.

The sum of all exponents is the *overall reaction order*. In order to classify reaction one uses the overall reaction order. To calculate the concentration [A] one needs to integrate equation 2.2 over time. Without loss of generality every involved species is also time-dependent which due to non-linearities makes it impossible to determine a general analytic solution for eq. 2.2. Actually the rate law needs to be formulated for all involved species, leading to a system of n ordinary differential equations.

However, in many instances species are in excess. Due to no major change in excess concentrations one can simplify eq. 2.2 by combining  $k' = k * [B]^b * [C]^c$ .. resulting to

$$\frac{d[A]}{dt} = -k' * [A]^a \tag{2.3}$$

In this species excess case, the exponent a simply defines the reaction order. Typical cases, such as a = 1 (leading to a first-order reaction) or a = 2 (leading to a second-order reaction) are well studied in literature and one can easily find analytical solutions.

However, reactions run forward and backwards which makes chemical kinetics analysis not that trivial. When the forward reaction rate equals the backward reaction rate one obtains chemical equilibrium [22, 24].

At equilibrium conditions, forward and backward reaction react equally fast, i.e.

$$0 = -k^{forward}[A]^{a}[B]^{b} * ... + k^{backward}[C]^{c}[D]^{d} * ...$$
 (2.4)

The equilibrium constant can be defined with indicated temperature dependencies as

$$K_c(T) = \frac{[C]^c [D]^d}{[A]^a [B]^b} = \frac{k^{forward}(T)}{k^{backward}(T)}$$
(2.5)

In a general setup, with the stoichiometric coefficients  $v_i^{forward}$  and  $v_i^{backward}$  which are identical to reaction orders the equilibrium constant can be expressed as

$$K_{c} = \frac{\prod_{products} [S_{k}]^{V_{k}^{backward}}}{\prod_{reactants} [S_{k}]^{V_{k}^{forward}}}$$
(2.6)

This equilibrium constant can be also expressed in terms of Gibb's free energy which is not discussed here in detail. Furthermore, one can calculate the backward rate coefficient knowing the equilibrium constant and the forward rate [22].

#### **Bimolecular reactions**

To give a detailed description of the combustion chemistry it is necessary to include not only overall reactions but all elementary reactions of the reaction mechanism. The representation of all intermediate species is essential. Elementary reactions occur exactly in the way as the reaction equation defines the molecular formations. As a consequence only whole integer numbers appear as stoichiometric coefficients  $v_i$  in the reaction and thus also as individual reaction orders.

Combustion processes consist mainly of bimolecular reactions and thus they are explained in the following.

A general bimolecular equation is given by

$$A + B \xrightarrow{k} C + D \tag{2.7}$$

Consequentially, the reaction rate is defined as

$$\frac{d[A]}{dt} = -k * [A] * [B]$$
 (2.8)

Bimolecular reactions run according to a second-order rate reaction (see previous section). Reaction coefficients for bimolecular reactions have a theoretical basis whereas global rate coefficients emerge from measurements. The collision theory for instance uses concepts of mean free path, mean molecular speed and wall collision frequency and thus, one can derive a theoretically justified state-dependent rate coefficient. However, this simplified view does not provide information about involved factors (e.g. activation energy, steric factor etc.). More detailed theories are necessary to describe the spatial forms of molecules and consequential bond breaking and forming. Currently, because of weaknesses of theories and its complexities it is common to use a three-parameter function for rate coefficients:

$$k(T) = A * T^b * \exp(\frac{-E_A}{R * T})$$
 (2.9)

with R representing the universal gas constant. A, b &  $E_A$  are empirical parameters that are tabulated for important reaction mechanisms and test conditions. When using such tabulated mechanisms one must keep in mind that these parameters are verified and validated for specified test conditions only [22]. (See also 2.1.2)

#### **Pressure and Temperature Dependence of Reaction Coefficient**

Whether a reaction occurs or not and how fast it advances depends non-linearly on temperature and pressure. The temperature dependence was described by Arrhenius (1889) with the exponential formula known as the Arrhenius law:

$$k(T) = A' * \exp(\frac{-E_A}{R * T})$$
 (2.10)

As stated before, currently in simulation setups equation 2.9 is preferred as it corresponds to the exponential dependence as well as a temperature factor fitted to measurements.

In general, elementary reaction rate coefficients do not depend on pressure. However, one observes a pressure dependence for a whole chemical process. Varying pressure influences species concentrations. These intermediate steps are not covered by a global reaction. When dealing with a detailed chemical mechanism (elementary reactions) rates are driven by species concentrations.

The Lindemann model explains reasons behind different formation rates at varying pressure for global reactions. In a decomposition reaction an excited molecule can either react back to the original state or form the product. This process is influenced by species concentration means. Reaction pressure dependence is strongly dependent on the reaction itself. It can easily be observed by comparing high- and low-pressure conditions for a global chemical reaction.

The previous mentioned functional dependencies can be explained with the activation energy. Reactants have to overcome an energy barrier in order to form the products. This barrier is called activation energy. In detail, this is a result of required bond splitting to initialize the reaction. A higher internal energy (caused by temperature or pressure) consequentially results in a faster advancing reaction. In fact, such dependencies must be examined in detail as different reaction paths are favored at different test conditions [24].

#### 2.1.2 Reaction Mechanisms

Global reactions may serve for an energy estimate of a combustion but are not sufficient for the calculation of pollutant concentrations. Combustion characteristics are driven by reaction paths with many elementary reactions and intermediate species. For hydrocarbon combustion detailed reaction mechanisms are developed that cover more than 110 chemical species and 600 reactions. Especially in a three-dimensional model this can lead to an enormous amount of computational work. Therefore, for a 3-D setup simplifications of the chemical mechanism are necessary [24].

The simulations in this thesis use the chemistry of the *GRI3.0-mech* with 53 species and 325 reactions. It is a detailed reaction combustion model for hydrocarbon flames including its elementary reactions and is developed by Berkeley University and sponsored by the Gas Research Institute. [5]

### **Aggregate Chemical Kinetics**

A detailed chemical mechanism, such as the *GRI3.0-Mech*, represents a chemical system of N species and M reactions. Hence, every possible occurring reaction j=1,...,M is specified:

$$\sum_{k=1}^{N} v_{kj}^{before} S_k \rightleftharpoons \sum_{k=1}^{N} v_{kj}^{after} S_k$$
 (2.11)

 $S_k$  represent species k and  $v_{kj}$  the molar stoichiometric coefficients of species k in reaction j. A reaction progress rate  $\Psi_j$  of reaction j can be defined with rate laws pointed out in section 2.1.1 including forward and backward occurring reactions.

$$\Psi_{j} = k_{j}^{forward} \prod_{k=1}^{N} [S_{k}]^{v_{kj}^{before}} - k_{j}^{backward} \prod_{k=1}^{N} [S_{k}]^{v_{kj}^{after}}$$
(2.12)

Individual reaction rates  $\dot{\omega}_{kj}$  can be formulated according to section 2.1.1, whereas  $\omega_k$  is an overall (summed up) reaction rate producing species k.

$$\dot{\omega}_k = \sum_{j=1}^{M} \dot{\omega}_{kj} = W_k \sum_{j=1}^{M} v_{kj} \Psi_j$$
 (2.13)

where  $\Psi_j = \frac{\dot{\omega}_{kj}}{W_k v_{kj}}$  is the progress rate and  $\dot{\omega}_{kj} = \dot{\omega}_{kj}^{after} - \dot{\omega}_{kj}^{before}$ .  $W_k$  denotes the molecular weights of species k.

In this system mass is conserved, whereas species might appear bound in molecules different to the molecules prior to the reaction. As a matter of fact, species atoms are conserved which provides N constitutive equations that are necessary for problem closure (See latter section 2.1.3). Mass conservation for all reactions j enforces

$$\sum_{k=1}^{N} v_{kj}^{before} W_k = \sum_{k=1}^{N} v_{kj}^{after} W_k$$
 (2.14)

Together with equation 2.13 one can derive that the summed rates of all reactions equals zero.

$$\sum_{k=1}^{N} \dot{\omega}_k = \sum_{j=1}^{M} (\Psi_j \sum_{k=1}^{N} W_k v_{kj}) = 0$$
 (2.15)

Given some assumptions the general reaction mechnaism can be simplified. In the following two common techniques are discussed.

### **Quasi-Steady State assumption**

Considering a chain mechanism including three species A,B,C with e.g. the reactions

$$A \xrightarrow{k_{12}} B \xrightarrow{k_{23}} C \tag{2.16}$$

Subsequently one can formulate the rate law according to

$$\frac{d[A]}{dt} = -k_{12} * [A] \tag{2.17}$$

$$\frac{d[B]}{dt} = k_{12} * [A] - k_{23} * [B]$$
 (2.18)

$$\frac{d[C]}{dt} = k_{23} * [B] \tag{2.19}$$

If one assumes species B to be very reactive the quasi-steady state assumption can be applied

$$\frac{d[B]}{dt} = k_{12} * [A] - k_{23} * [B] \approx 0$$
 (2.20)

Subsequently, equation 2.19 can be simplified to

$$\frac{d[C]}{dt} = k_{12} * [A] (2.21)$$

In general, this approximate steady state assumption can simplify the calculations. Species C is only dependent on species A. Obtaining a solution with this technique demands less computations than the coupled general setup [24].

### **Partial Equilibrium Assumption**

At sufficiently high temperatures reactions occur so fast that one can assume partial equilibrium to be reached. This is the case if forward and backward reaction speeds are equal.

Again, one can obtain a simplified, approximate solution saving computational effort. The procedure is fairly straightforward. For all involved reactions the rate law must be formulated. One ends up with a system of equations that can be solved for the species concentrations.

For high temperatures, the assumption calculates results similar to the detailed chemistry.

### 2.1.3 Modeling of Laminar Premixed Flames

The model of a Laminar Premixed Flame assumes a flow with specified inlet conditions and a propagating laminar flame. In most flame configurations pressure changes and viscous heating are negligible and body forces are zero. Besides, a steady state solution of the calculation is desired as also steady conditions are present in the gas turbine. As a consequence, the following simplified conservation equations can be derived:

- Mass conservation

$$\rho u = constant = \rho_1 s_L$$

- Species conservation (k=1...n)

$$\frac{\partial}{\partial x}(\rho(u+V_k)Y_k) = \dot{\omega}_k$$

- Energy conservation

$$\rho C_p u \frac{\partial T}{\partial x} = \dot{\omega}_T + \frac{\partial}{\partial x} (\lambda \frac{\partial T}{\partial x}) - \frac{\partial T}{\partial x} (\sum_{k=1}^n C_{p,k} Y_k V_k)$$

with 
$$\dot{\omega}_T = -\sum_{k=1}^N h_k \dot{\omega}_k$$

Furthermore, models for the reaction rate  $\dot{\omega}_k$  (See 2.1.2) and diffusion velocity  $V_k$  (e.g. Velocity correction by Fick's law, see below) are necessary to close this set of equations. Characteristics of closing terms are explained further below.

For calculating an unique solution boundary conditions, such as inlet temperature and species composition, need to be specified. To ensure that an ignited flame exists in the domain an additional, computational boundary condition must be imposed. Therefore, one assumes the outlet temperature to reach the adiabatic flame temperature which can easily be evaluated by an energy balance. However, some pollutant reactions do not reach chemical equilibrium conditions.

#### Reaction rate closing terms

The reacting flow with the above mentioned conservation equations also requires a model to calculate the reaction rate and the diffusion terms.

Species concentrations are iteratively calculated using the reaction rates as specified in 2.1.2. However, species concentrations diffuse simultaneously in the domain. Additionally a mass balance including one species arise further difficulties since the flow is reacting. Hence, an iteration is essential to approach to the solution.

For calculating diffusion velocities a few simplifications have to be made in order to reduce computation effort. In most premixed setups the Soret effect (mass diffusion induced by temperature gradients), pressure gradients and volume forces are neglected [16]. Fick's law describes the mass diffusion to be solely proportional to the concentration gradient:

$$j_{m} = \frac{\partial m}{\partial t * Area} = -DM \frac{\partial c}{\partial z}$$
 (2.22)

where M is the molar Mass,  $j_m$  the concentration mass flux and D the factor of proportionality. D can be experimentally measured as particle movement of labeled isotopes [24].

However, the mass diffusion can further be simplified by approximating Fick's law with the Hirschfelder and Curtis approximation. Basically this approximation involves a first-order expansion and is exact for the binary diffusion case. For the multi-species setup approximative errors are unavoidable.

Furthermore often the simplest approach for solving the global mass conservation is chosen. Therefore the continuity equation is solved for N-1 species. To round of any error, the last species is obtained by writing  $Y_N = 1 - \sum_{k=1}^{N-1} Y_k$  [16].

#### Convergence radii of One-dimensional Free Flames

A steady solution exists only if the inlet velocity of the grid equals the laminar flame speed  $s_L$ . The code tries to iteratively approach to this value.

Therefore, the used *Cantera* module calculates a first flame solution in terms of temperature field and concentration fields of species  $Y_k$ . Then it refines the finite-difference grid at regions of high gradients. The system is subsequently solved with Newton's method.

If these fields vary too far from the solution, the code does not converge to the solution. When dealing with parameter variations, the method of continuation seems appealing. The solution of the previous case is used to initialize the flame [16, 24].

### 2.1.4 Perfectly Stirred Reactor (PSR)

For the construction of a modeling tool, a network of reactors is often used. Flow information is obtained from a CFD simulation. Thereafter a reactor model is developed accordingly to describe the combustion chemistry and to predict pollutant formation. The big advantage of these tools in comparison with Free Flame simulations is that Reactor Networks produce prompt and reliable results with reasonable computational effort. The calculation of Free Flames on the other hand is very tedious and therefore not suitable for industry usage. Especially a detailed mechanism of hydrocarbon combustion coupled with 3D flow fields exceeds typical CPU capacities. The calculation of pollutant formation requires the full chemistry and thus, many flame specialist suggest the use of a reactor network [6, 7].

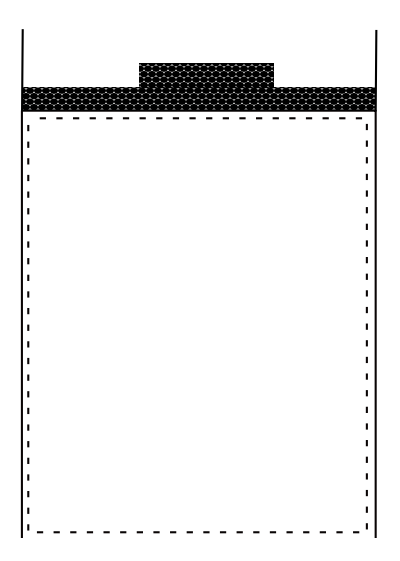


Figure 2.1: Schematic of a constant pressure, constant mass reactor

### **Characteristics of a Perfectly Stirred Reactor**

Defined by the name, a perfectly stirred reactor assumes a perfectly mixed configuration inside the reactor and the fluid to be homogeneous in composition as one phase mixture. As a result mass diffusion and other flow descriptions are omitted. In above mentioned tools, such effects are considered in the developed reactor model. The flow domain is divided in separate regions. These regions are distinguished in a way that a homogeneous mixture can be assumed [7, 16].

In the simulation a constant-pressure, fixed mass reactor is utilized; hence this particular setup is discussed in detail.

#### **Constant Pressure, Constant Mass Reactor**

In this type of reactor temperature, pressure, composition and reaction rate are the same at every location of the batch. The described setup is displayed in figure 2.1. The piston on the top can move to equalize the pressure inside. In contrast to the Free Flame simulations, one can observe time-advancing reaction phenomena. Surely, after a certain period of time the PSR will also reach steady state.

The equations of state for the reactor are reduced to a system of first-order ordinary differential equations (ODE). The species' state only depends on the initial value, i.e. the species inlet composition and its temperature [22].

By applying energy conservation, ideal gas behaviour and a model for species formation one ends up with a ODE for the batch's temperature as shown in Turns [22].

$$\frac{dT}{dt} = \frac{(\dot{Q}/V) - \sum_{k} \bar{h}_{k} \dot{\omega}_{k}}{\sum_{k} ([S_{k}] \bar{C}_{p,k})}$$
(2.23)

Again,  $\dot{\omega}_k$  symbolizes the species production by the chemical mechanism; the bar denotes an average between actual temperature and reference temperature.

Similarly, species concentrations  $[S_k]$  can be expressed by an ODE derived by mass conservation, constant pressure and ideal gas law.

$$\frac{d[S_k]}{dt} = \dot{\omega}_k - [S_k] \left( \frac{\sum \dot{\omega}_k}{\sum_l [S_l]} + \frac{1}{T} \frac{dT}{dt} \right) \tag{2.24}$$

The derived expressions are functions of temperature and concentrations only. However, when defining the system one can also specify a certain heat transfer. The Cantera module offers different possibilities, such as heat transfer coefficients or wall heat flux [8].

A stiff solver is advisable since components usually differ in orders of magnitude [22].

In conclusion, Perfectly Stirred Reactors reduce the model drastically, but offer the opportunity to acquire a fast and accurate result using detailed chemistry. By considering information about the flow one can derive a smart network of these reactors and still portray the experimental setup. Finally, prompt and reliable pollutant information can be obtained for imposed conditions, where no experiments are conducted [6, 22].

### **2.2** Reaction Mechanisms of $NO_x$ formation

Nitric Oxides in the exhaust gas of combustion originate from complex formation mechanisms. Thus, a solely experimental study is not sufficient in understanding the complex processes in pollutant formation [24].

 $NO_x$  concentrations mainly consist of nitrogen oxide (NO) and nitrogen dioxide ( $NO_2$ ). Typically NO-values dominate in emission measurements [9].

For natural gas combustion systems  $NO_x$  is mainly formed by these four mechanisms:

- Thermal/Zel'dovich mechanism
- Prompt/Fenimore mechanism
- NNH mechanism
- N<sub>2</sub>O mechanism

The Thermal and the Prompt mechanism contribute most to  $NO_x$  emissions at test conditions; hence they are precisely described in the following chapter.

### 2.2.1 Thermal/Zel'dovich Mechanism

In technical applications a considerable amount of  $NO_x$  is formed through the Thermal/Zel'dovich reaction path. It has been first described by Y.B.Zel'dovich in 1947 and involves the following reactions:

$$N_2 + O \stackrel{k_1}{\rightleftharpoons} NO + N \qquad E_A = -318kJ \tag{2.25}$$

$$N + O_2 \stackrel{k_2}{\rightleftharpoons} NO + O \qquad E_A = -26kJ \tag{2.26}$$

$$N + OH \stackrel{k_3}{\rightleftharpoons} NO + H \qquad E_A \simeq 0kJ$$
 (2.27)

The mechanism is also often referred as the thermal pathway of NO formation because of its strong temperature dependence. Reaction kinetics are driven by the reaction rate coefficients  $k_{1/2/3}$  and the concentrations of  $O_2$ , O and OH. A simple comparison of activation energies reveals that reaction 2.25 is much slower than the others. Activation energies influence the reaction rate coefficient significantly. Hence, as shown by Turns, Reaction 2.25 is the rate determining step [22, 24].

Atmospheric  $N_2$  is attacked by oxygen radicals present in combustion and nitrogen oxide and highly atomic nitrogen is formed. This N radical is also further decomposed to NO in reaction 2.26 and 2.27. Therefore, especially the concentration of atomic oxygen govern the thermal  $NO_x$  production.

In detail, the strong temperature dependency is caused by increasing O-concentrations with rising temperature and the high activation energy for decomposing the  $N_2$  triple bond. In the flame front, atomic oxygen concentrations (O) well above thermodynamic equilibrium concentration result in higher formation rates than in regions downstream. These elevated radical concentrations in the flame front are called super-equilibrium conditions.

However, caused by the slow reaction 2.25,  $NO_x$  values rise further in the postflame zone with longer residence times.[9, 10, 22] In emission concentration measurements chemical equilibrium cannot be assumed as it is reached in time scales that vary widely from residence times in the combustion chamber. Thermal NO is therefore mainly a function dependent on temperature and residence time. [13, 24]

### 2.2.2 Prompt/Fenimore Mechanism

The thermal pathway has been identified prior to the prompt<sup>1</sup> pathway and has long been thought to be the only contribution to  $NO_x$  emissions. However in the 1970s, C.P. Fenimore observed higher NO-values in the combustion of hydrocarbons in fuel-rich regimes( $\Phi > 0.8$ ) than predicted by the thermal pathway [2, 9]. He postulated the formation mechanism of promptly produced NO by CH radicals (and similar radicals) which are intermediate molecules in the flame front. Together with nitrogen hydrocyanic acid (HCN) is formed [24]; the following reactions are included: [9]

$$CH + N_2 \rightleftharpoons HCN + N \tag{2.28}$$

$$CH_2 + N_2 \rightleftharpoons HCN + NH \tag{2.29}$$

In more complicated mechanisms HCN reacts subsequently to NO,  $N_2$  and other species. Yet the preceding reactions (2.28 and 2.29) are rate limiting. Contrary to thermal NO, the prompt reaction path is still active at relatively low combustion temperatures [24].

### 2.2.3 Other Mechanisms

There are several other possible ways of  $NO_x$  formation. Depending on the combustion conditions the effect of the reaction mechanism on the pollutant formation changes. Hereafter,

<sup>&</sup>lt;sup>1</sup>The description "Prompt" originates from the short lifetime of intermediate radicals involved in the reactions. [10]

mechanisms with a minor influence are described.

### **NO** production by Nitrous Oxide $N_2O$

In the  $N_2O$  mechanism the strong Nitrogen  $N_2$  triple bond is split with atomic oxygen O in the presence of a third species to form  $N_2O$ . The Nitrous Oxide  $N_2O$  is converted subsequently to NO with O-and H-radicals. This depletion reaction often takes place in the post-flame zone. In the investigated scenarios this mechanism was of minor relevance [10, 24].

#### **NNH** mechanism

Bozzelli and Dean[3] proposed an additional reaction path for NO-models that contributes remarkably to  $NO_x$  formation in regions of high atomic hydrogen and atomic oxygen O concentrations such as flame fronts. Nitrogen molecules are attacked by hydrogen radicals to form NNH. Thereafter, NNH is decomposed with oxygen O radicals to NO [3].

#### Fuel NO

Fuel NO (also often referred to by FBN: fuel-bound nitrogen) is formed by nitrogen that is bound with fuel molecules. On the one hand, this FBN plays a major role in coal combustion since even in 'clean' coal 1 mass-% nitrogen is bound chemically. On the other hand, some combustion gases consists of fractions of ammonia which leads to the FBN [10].

Firstly, a model for the Nitrogen release from the fuel molecules has to be introduced. Secondly, a formation mechanism for released Nitrogen-species needs to be specified to model FBN  $NO_x$  formation. Also, these steps require additional knowledge about the fuel species; for example coal compositions can vary significantly. Consequentially many different individual formation routes are developed for describing the  $NO_x$  release by Fuel-bound Nitrogen. Nitrogen bonds within the fuel are weaker than triple nitrogen bonds for atmospheric Nitrogen; as a result the reaction decomposing FBN has a lower activation energy. For fuel that contains FBN this is the dominant formation mechanism [9].

The test fuel has no nitrogen bound in fuel molecules. However, the burner can also operate with flexible fuel. Therefore, in order to describe nitrogen oxide formation sufficiently Fuel NO should be taken into consideration as well [21].

# 3 Methodology

In the following chapter the basic methodology for the developed numerical tool is described. In a first step Free Flame simulations are conducted to analyze the basic influence of water injection in flames. In a second step a reactor network is established which uses provided data from preceding Free Flame Calculations. Hereby, CFD data is also consulted to calculate particle residence times.

The calculations are conducted with the *Cantera 2.1* module for *Python 3.3*. Implemented code is available on an attached CD and step-by-step instructions are given in the appendix for interested readers.

On the one hand, a scenario is investigated where water is injected while keeping the equivalence ratio constant. A decline in temperature is expected. On the other hand, the equivalence ratio is adjusted in a way that the temperature is kept constant.

### 3.1 Description of the experimental setup

### 3.1.1 Experimental test rig

A schematic of the experimental setup corresponding to the numerical tool is displayed in figure 3.1.

First, ambient air is preheated; then fuel is added to the flow in a mixer. The ambient air is preheated to temperatures so that after the mixer desired 'fuel-air' mixture temperatures are attained. The preheater can establish unburned mixture temperatures up to 400°C.

Secondly, the mixture enters the burner. The burner consists of a conical swirler followed by a convergent tube. A schematic of the burner is depicted in figure 3.2. A certain fraction of the mixture flows through an circular gap at the top of the cone. The remaining mixture passes

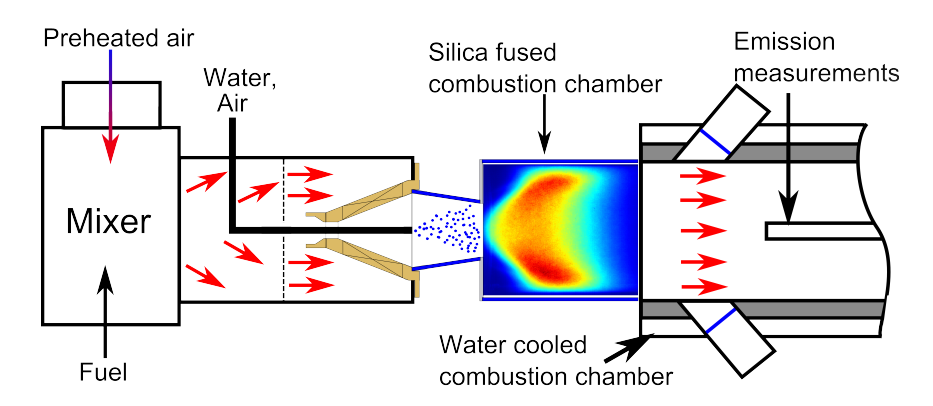


Figure 3.1: Experimental test rig [14]

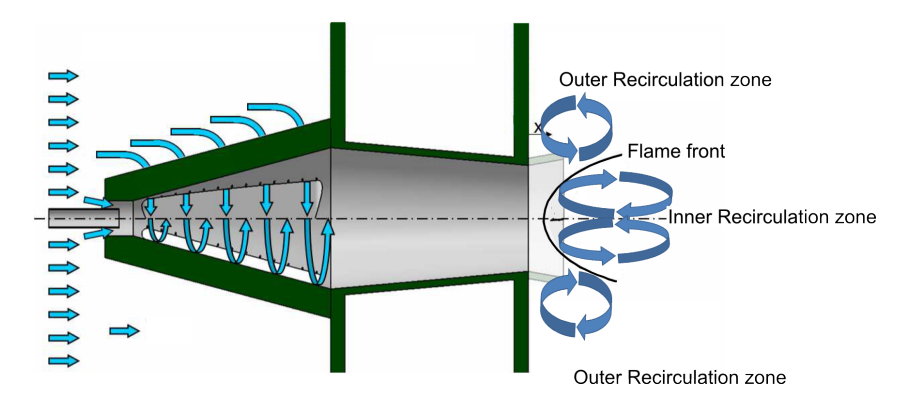


Figure 3.2: Schematic of the burner - Recirculation zones in the combustion chamber [19]

the conical swirler. The swirler includes a thick walled hollow cone with four tangential slits that are equally spaced around the circumference. Hence, a vortex is induced in the flow. The mixture fraction through the gap at the cone's apex preserves axial momentum.

Subsequently the mixture flows into a combustion chamber where the flame front is located. A sudden change in cross-sectional area forms a recirculation zone. The flame front is stabilized between an inner and outer recirculation zone as described in the following section 3.1.2.

Silica fused walls delimit the beginning of the combustion chamber (see figure 3.1). A water cooling mechanism is subsequently attached. The emission probe is located approximately 0.5m downstream of the flame. Concentration measurements are collected with a centrally aligned tube [11].

### 3.1.2 Flame stabilization methods

Flame stabilization plays a major role in combustion research because a stabilized flame significantly extends the lifetime of a burner as well as improves safety arrangements.

The basic idea is to create regions of low flow velocity taking into account that the flow velocity is smaller than or equal to the flame speed. One might think of inducing a stagnation and recirculation zone in the burner using a perforated plate or rods. Nowadays, state of the art is an aerodynamic stabilization of the flame. In the investigated burner the fuel-air mixture passes a swirler upstream and forms a recirculation zone in the combustion chamber (see figure 3.2)[12].

In the combustion chamber an inner and an outer recirculation zone is formed. The flame front is located between the recirculation zones. Thus, a propagation of the flame front is prohibited and the flame remains stable at the same location.

### 3.1.3 Water injection

The water injection method is still a subject of development and further improvements are deemed necessary. The current setup is described below:

Water is injected through a pipe centrally aligned in the burner. It reaches to the transition of the conical swirler and convergent tube.

In general, liquid water is injected using a nozzle at the tube outlet. One tries to atomize the droplets, so that a homogeneous and gaseous mixture is attained prior to combustion. For high temperatures through temperature diffusion of the flame front and by preheating these objectives are fulfilled in good agreement for small water injection rates. However, the water injection method is a design task which might be improved in the course of the project.

For the numerical simulation a perfectly premixed fuel-air-water solution is assumed. The reason for this gaseous approximation is that the PREMIX solver of Cantera cannot handle a two-phase mixture. Surface reactions on droplets are very difficult to handle numerically. Additionally, droplet surfaces have fairly low temperatures (~ 100°C), thus reactions are very slow and negligible.

The temperature of this reactant mixture is set to the preheat value in the numerical calculation. This assumption raises concerns about the validity of the simulation tool. In the experimental setup the vaporization of the water will definitely cool down the mixture before combustion to a value significantly below the preheat value.

However, this only plays a role in the setup where temperature declines as water is injected. By taking a higher value for the temperature the tool constantly over-predicts the  $NO_x$  formation and an upper  $NO_x$  bound is obtained.

In the setup constant flame temperatures for water injection approximately the same flame temperature is reached in the experiment as well in the numerical setup. However, different equivalence ratios are obtained comparing the both cases. The reason is simply the vaporization enthalpy. Obviously the tool calculates a smaller equivalence ratio than the one applied in the experiments. In conclusion, in this case flame temperatures are nevertheless similar, but mixture composition varies.

For a more accurate numerical prediction the temperature of the mixture at the combustion chamber inlet needs to be determined. Either one could approximate the temperature with an energy balance; however this is not accurate since temperature diffusion upstream is difficult to approximate. Or a temperature measurement at the combustion chamber inlet is helpful in correlating numerical and experimental results. However, a physical thermocouple sensor significantly influences the flow field and the flame. Similarly a measurement of the flame temperature is difficult. A thermocouple would change the flow conditions. Under these circumstances the simplifications mentioned above are made. These assumptions are also considered in the discussion of the results.

### 3.1.4 Combustion chamber cooling and emission measurements

The atmospheric test rig is described in section 3.1.1. In the following heat release by the test rig is discussed.

Ambient air convectively cools down the fused silica walls of the combustion chamber (see figure 3.1). Simultaneously radiative heat transfer is occurring through the transparent fused silica delimitations. The attached non-transparent walls of the combustion chamber are cooled by pumped water. Emission measurements are measured downstream inside the water cooled part of the combustion chamber as shown in figure 3.1.

At this point, again a few words about the numerical model are necessary. The Free Flames are adiabatic, whereas in the test rig the flame front is cooled (notably also by radiative emis-

sions). Furthermore, in the reactor network for the post-flame zone a heat removal can be incorporated accordingly if the heat removal rate is known. For the test rig it is very difficult to estimate the heat release by cooling mechanisms of the burner system. A considerable amount of heat is removed by the water cooling mechanism. Although the inlet and outlet temperatures of the water can be estimated, the mass flux and hence the heat removal is unknown. Also, an estimate of the emitted radiation of the flame is rather imprecise. The easiest way of evaluating the overall heat transfer would be temperature measurements at the burner inlet and at emission probe location. However, for that purpose the test rig would need to be reconstructed regarding these concerns. Currently, a possible estimation of the heat removal is very vague.

### 3.2 One-dimensional Free Flame

To investigate the chemical processes more thoroughly, two numerical simulation tools of the combustion chemistry are developed. The fuel and air compositions for all measurements are summarized in table 3.1.

Mixture compositions			
	$CH_4$	96.96 <i>Mol</i> .%	
	$C_2H_6$	$1.93\ Mol.\%$	
Fuel	$N_2$	$0.62\ Mol.\%$	
	$C_3H_8$	0.26Mol.%	
	$CO_2$	$0.23\ Mol.\%$	
Air	$N_2$	79 <i>Mol</i> .%	
All	$O_2$	21~Mol.%	

Table 3.1: Species compositions of air and fuel used for all simulations

The data are average measurements by the gas company for provided natural gas [21]. Since atmospheric Argon ( $\sim 1\%$  in atmospheric air) is inert, for simplicity the  $N_2$  concentration is taken as 79%.

### 3.2.1 Measurement points

Furthermore series of measurements are performed to investigate many different cases and dependencies of the  $NO_x$  formation. Hereby, different amounts of water are injected into the combustion chamber. One can define the water-to-fuel ratio as  $\Omega = \frac{m_{water}}{m_{fuel}}$ . Calculations are carried out for different water injection rates and variable preheat temperatures. Measurement points are defined in table 3.2.

With a measurement series, at first the equivalence ratio is kept constant whilst increasing  $\Omega$ . In a second step the flame temperature is held constant with rising water proportions. Therefore, the equivalence ratio is increased resulting in a constant flame temperature for rising  $\Omega$ .

T 11 00 0	C	11.1	• •	
Table 3.2: Summary	7 Of test co	nditions for	ceries of m	pacurements
Table 3.2. Sullillial	or itsi to	munuons ioi	SCITCS OF THE	casarcincins

Test conditions		
Pressure p	$1.0 * 10^5 $ Pa	
	1.4	
	1.5	
	1.6	
Inverse Equivalence Ratio $\frac{1}{\Phi}$	1.7	
-	1.8	
	1.9	
	2.0	
	0	
	0.25	
	0.5	
Water injection ratio $\Omega$	0.75	
	1.0	
	1.25	
	1.5	
	673 K	
Prohoat tomporature T	573 K	
Preheat temperature $T_{pre}$	473 K	
	373 K	

Additionally, a certain initial mass flux  $\dot{m} = 0.005 kg/s$  is at the inlet of the domain. However, this is adjusted in the solution calculation accordingly to fulfill the equation  $\dot{m} = \rho_1 s_L$  (See also section 2.1.3).

### 3.2.2 Simulation Steps

For the simulation the software package *Cantera* is used. *Cantera* is a software tool to solve problems involving diffusions, thermodynamics, and chemical kinetics [8]. The code is implemented in the *Python 3.3* programming language with functions offered by *Cantera*. For reaction kinetics calculations *Cantera* made use of the *GRI-Mech3.0*, a database for hydrocarbon combustion reactions [5]. Postprocessing (e.g. normalizing) data was performed on *MATLAB R2014a*.

The basic procedure for Free Flames in *Cantera* is applied. A gas object is created using a *GRI3.0-Mech* solution. Herby, the species molar fractions are defined according to table 3.1 and injected water corresponding to table 3.2. The pressure and preheat temperatures are specified in table 3.2. In the case of constant flame temperatures, a modification of the equivalence ratio is necessary. A simple iteration with rising fuel proportion is implemented, whereas the flame temperature is calculated by the equilibrate function provided by *Cantera*. As soon as the desired temperature of dry case is reached, the adiabatic Free Flame simulation is started.

A Free Flame object is initialized including a initial grid that is imposed by the user. Bound-

ary conditions are set to the unburned mixture at the inlet and the computational constraint of equilibrium temperature at the outlet to ensure that flame is ignited (see 2.1.3). A first flame solution is then presumed with a linear temperature profile. To prevent the flame from moving outside the domain, a certain temperature  $T_{fix}$  is set at a discretization point in the center of the Free Flame domain. In the *Cantera version 2.1* this temperature is  $T_{fix} = \frac{T_{equil} - T_{inlet}}{2}$  [8]. In the following a constant refinement of the initial grid takes place until the final flame front solution is attained. The initial solution is approximated with neglecting the energy equation. In the next steps the energy conservation followed by multi-species diffusion processes are considered.  $^1$ 

There are many other options that can be imposed by the user: Setting maximum Jacobian age, residuals, or  $T_{fix}$ . A very high proportion of CPU time is consumed by the calculation of the Jacobian for the Newton solver. One can set the maximum age of the Jacobian Matrix to a certain value. However, this might lead to convergence issues and thus, the default value was used. In some cases, solving the problem first with a greater residual, then reducing the residual can increase the performance of the code. This method was used at several points in the series of measurements.

### 3.2.3 Post-processing

The python script creates an .xml file where the data during the simulation process is stored. After completion, a .csv file is generated with the numerical solution of all grid points. One might wonder which discretization point corresponds to experimental measurements. As stated in 2.2.1, thermal  $NO_x$  is progressively produced in the post flame zone and for emission measurements chemical equilibrium is not reached. In the .csv file for every discretization point also a flow velocity and a numerical one-dimensional distance is saved. Therefore, one can calculate the residence time point where experimental measurements are collected. However, the test rigs' distance is much greater than the computational domain of the Free flame. An adaptation of the numerical domain would lead to excessive CPU requirements. Hence, the Free Flame solutions serve as a well estimate, but for improvements and  $NO_x$  emission prediction a subsequent reactor network is applied.

### 3.2.4 Computation setup for series of measurements

Free Flame calculations have a high demand for CPU capacities and consume much time. Since almost 400 different operational points (Free Flames) are calculated an efficient, perhaps parallelized, computational setup is desired.

First of all, a simple conglomeration of for-loops was used to cover all operational points. In the case of constant flame temperatures, a matrix containing the inverse equivalence ratios was first calculated for each preheat temperature using the *equilbrate* function. Furthermore, whilst running the program on a standard computer one observes that only one core is employed. The office computer that is used consists of four cores. Therefore, the Python console was opened in four different windows on the PC to occupy all four cores simultaneously. Free

<sup>&</sup>lt;sup>1</sup>As stated in section 'Convergence radii' in 2.1.3, the calculation (time integration) fails if the numerical solution varies too far from the actual solution. In this case, a manual adjustment of  $\dot{m}$  or the initial grid is necessary.

flames of a particular case are still solved with one core but different measurement points were calculated at the same time on different cores.

### 3.3 Chemical Reactor Modeling

A three-dimensional chemical kinetics calculation demands a high amount of computational effort; the previously described One-dimensional Free Flame is insufficient in predicting  $NO_x$  concentrations. A reactor network is developed where flow information by a non-reacting CFD simulation is incorporated. The basic methodology is described below.

### 3.3.1 Reactor Network constructed by Residence Times

The special feature of the flow field in the combustion chamber is the induced swirl which form in an inner and an outer recirculation zone. The flame is formed in the space between these steady recirculation regions and thus the flame is stabilized. A sketch of the flow field is depicted in figure 3.2, section 3.1.1.

As stated in section 2.2.1 (thermal)  $NO_x$  concentrations are strongly dependent on residence times. Because of the recirculation zones particle residence times vary largely depending on whether they are delayed by a recirculation. Considering these circumstances a reactor network including a probability density function (PDF) of particles' residence times is utilized for  $NO_x$  prediction. A schematic of the methodology of the reactor network is depicted in figure 3.3.

One-dimensional Free Flame calculations are used to model the complex processes in the flame front. Particles cross the flame surface which can be seen as a one-dimensional event. This step is modeled by the One-dimensional Free Flame. Subsequently, a residence times distribution of particles in the combustion chamber is generated. To keep the computational efficiency high the residence times are sectioned into sectors with corresponding occurrences. Subsequently, for modeling the time dependent  $NO_x$  formation a perfectly stirred reactor (PSR) is used.

### 3.3.2 Particle Residence Time Calculation by CFD data

For the calculation of the particle residence time a Computational Fluid Dynamics (CFD) simulation of the burner geometry is essential. The calculations have been performed with *ANSYS*[1]. The particle residence time data is exported using a .csv file.

The CFD simulation uses ideal gas as a working fluid. Fichet et al. suggest to use a low-level reactive chemistry in the CFD-simulations [7]. However, prior experimental and theoretical knowledge reveal that the flame is formed in the space between the recirculation zones.

A surface between the recirculation zones was created by an isosurface setting the axial velocity constant. In reality, the velocity perpendicular to the flame surface is zero. Many difficulties arose when defining the surface in *ANSYS*. As a best guess, a surface is created connecting all points with axial velocity v=27 m/s. Since also discretization points in the swirler

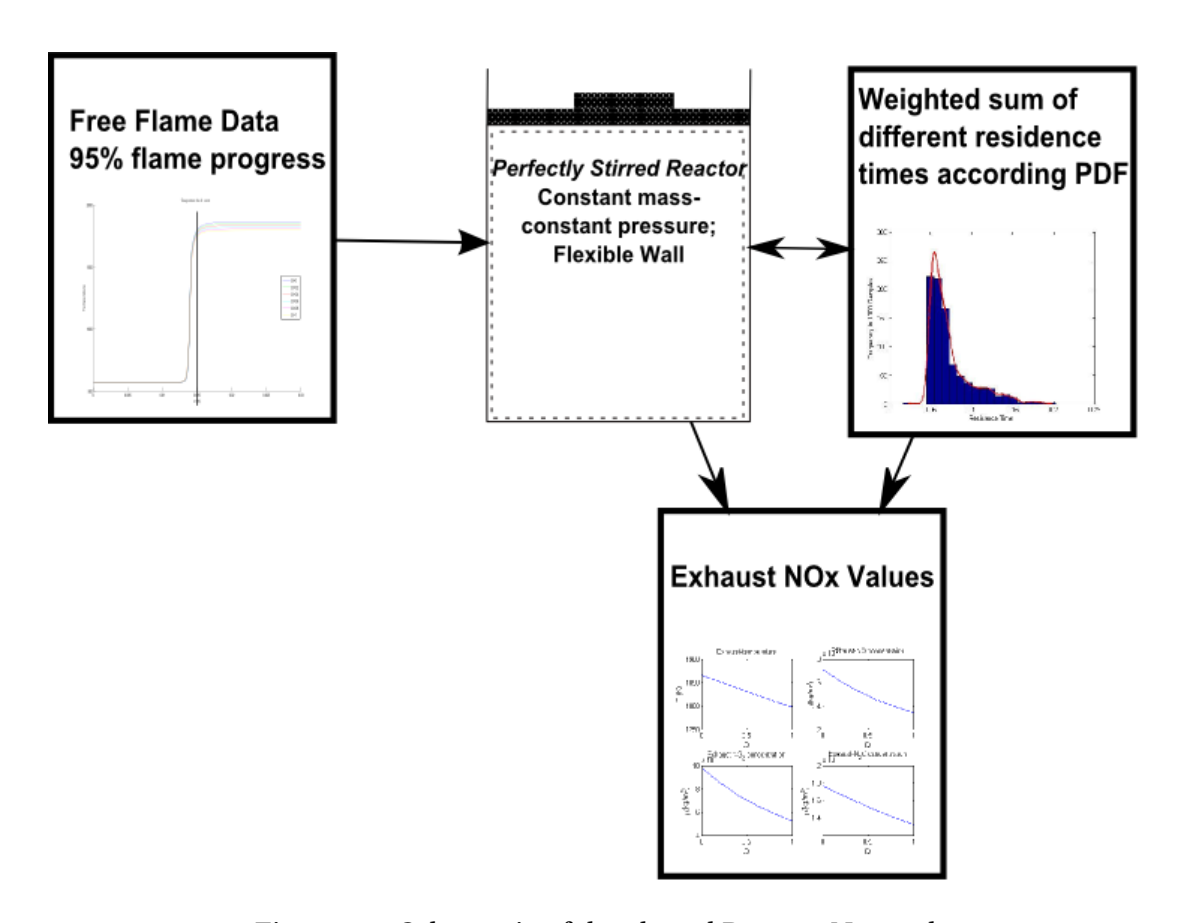
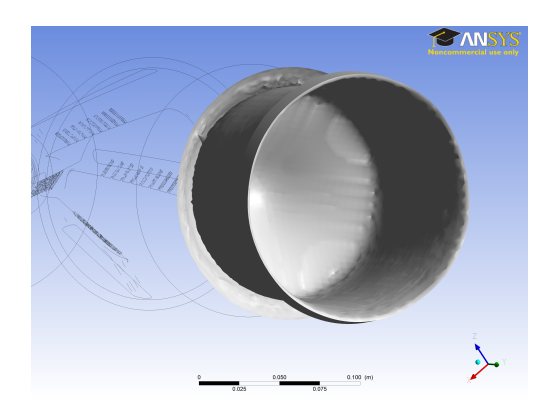


Figure 3.3: Schematic of developed Reactor Network

are selected, a part of the surface is disregarded. Hereby, *ANSYS* offers the function of Iso-Clips. Only the surface in the combustion chamber was selected by disregarding the domain with axial coordinate Y < 0.135m. The resulting surface is depicted in figure 3.4.



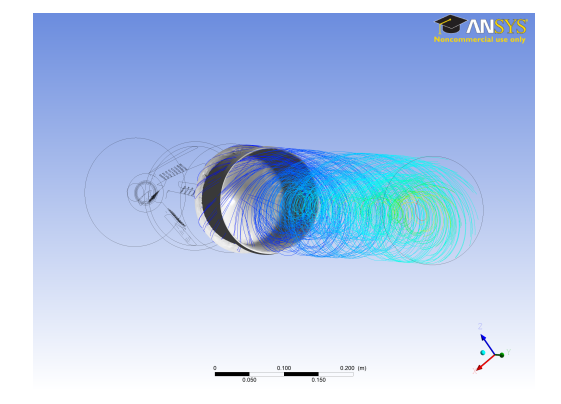


Figure 3.4: Flame front approximation by Isosurface in ANSYS

Figure 3.5: Trajectories of particles after crossing the isosurface

Afterwards particles are added to the flow the particle trajectories are calculated. The particles' material is solid aluminum. They are spheres of diameter 2e-3mm. The density was modified to an unphysical value for solids, i.e.  $1kg/m^3$ , in order to decrease inertia and to better follow the flow field. In total, a reasonable number of 1000 particles are used in order to attain a smooth and accurate probability density function. A sample of 200 trajectories for better visualization is displayed in figure 3.5

The residence times of particles can be calculated in *ANSYS*. They are seeded at the flame surface and end at the outlet where emission measurements are made. A .csv file is exported including a counter i and the residence time of particle i. The injected water is assumed to influence the flow field in a minor way. Therefore, the same residence time distribution is used for all operating modes.

### 3.3.3 Probability Density Distribution of Residence Times

For further analysis the .csv file of residence times is imported in *MATLAB*. A short data revision in the *MATLAB* code corrects unphysical values. Thereafter a probability density function is constructed partitioning the data in 20 sectors according to their occurrences. The *MATLAB* built-in function *histfit* is used to create a histogram with polynomial fit. It is depicted in figure 3.6 with the polynomial function fit drawn in red.

At the same time a mean value of the distribution is determined to be 74.1*ms*. However, this single value does not describe the distribution sufficiently. A weighted sum of the reactor concentrations at different residence times is more accurate than the mixture composition for the average residence time only.

One can observe high occurrences at residence times of approx. 50ms, but also few particles with higher residence time. Such particles are detained in recirculation zones. Others pass the combustion chamber straight without major delay.

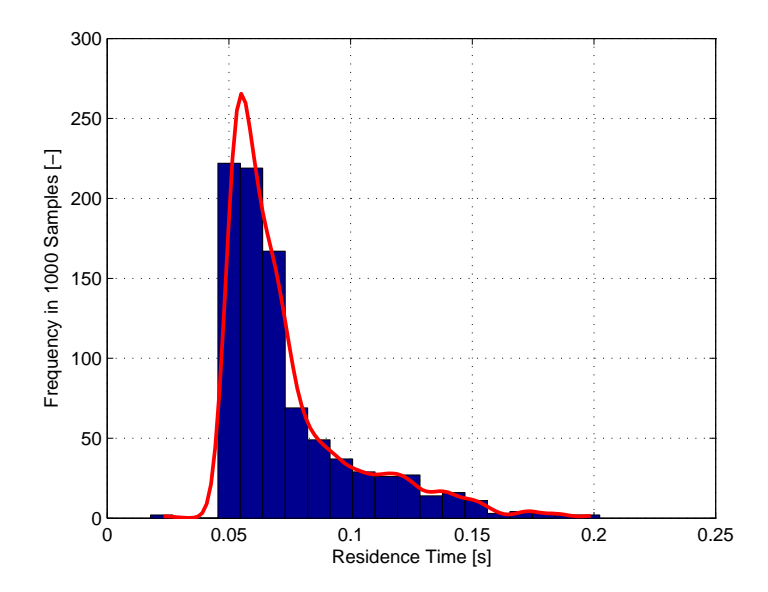


Figure 3.6: Probability distribution of particles' residence times in the combustor after "crossing" the flame- the polynomial fit in red, Histogram in blue

### 3.3.4 Computation setup for series of measurements

In order to structure the data, Free Flame data of the discretization point where the mixture has reached 95% of the equilibrium temperature are saved in .csv databases. A more detailed description on the procedure can be found in the appendix, section B.3.1. These databases contain the results of the Free Flame calculation when they reached 95% of  $T_{equil}$ .

One database contains the values for the test conditions and the mixtures' flame temperature (see table 3.3). In a second .csv file species compositions are saved. 53 species are included in the *GRImech3.0*. Thus, these concentration are saved as 53 comma separated values in another file.

2 different files are used for easier importing in *Python*. A schematic of the different csv files is given in table 3.3. Further descriptions are given in the appendix.

Table 3.3: Schematic of different .csv files for 95 % Free Flame data

Inv. Equiv. Ratio $\lambda$	Water inj. $\Omega$	$T_{pre}$	$T_{flame}$	Species molar fractions X
		•••	••••	,,,,,(53 Values)
			••••	,,,,,

Every row corresponds to a different measurement point and for each the Perfectly Stirred Reactor (PSR) must be initialized. An adiabatic perfectly stirred reactor with atmospheric pressure depends only on two specifications. First, this is the temperature at t = 0. Secondly, the composition of the 53 species must be defined (see 2.1.4).

The other values of the measurement point .csv files are used for structuring and saving the data. Time-advancing phenomena are modeled by calculating time steps in the reactor network until the highest possible residence time is reached. Thereafter a weighted average of the concentrations at different time steps is computed. Residence times of the sectored probability distribution and corresponding heights are used accordingly.

#### 3.3.5 Heat loss of the combustion chamber

Currently, no heat transfer is incorporated in the reactor network because of the difficulties in estimating the heat removal (see section 3.1.4). In reality, on the one hand the Free Flame is cooled down by radiative emission and convective heat transfer of the fused silica walls. On the other hand the water-cooling in the region attached to the silica walls cool down post flame zone. A temperature measurement in the combustion chamber would reveal information that could be incorporated in the reactor network.

For these reasons one must keep in mind that the tool constantly over-predicts the  $NO_x$  emissions because of higher resulting flame temperatures. However, for dry conditions the heat removal factor can be estimated by comparing experimental and numerical  $NO_x$  values. When incorporating this heat removal for other measurement points one attains a good match between numerical estimation and experiment. Since this factor misses a theoretical justification the tool is chosen to be adiabatic. If a proper estimate of the heat removal is found, it can be implemented easily in the tool.

Furthermore a model of the combustion-cooling by water injections needs to found. By taking the preheat value of the air as inlet temperature again an error in the temperature profile is made This is only present in the case of constant equilibrium ratios. This adds up to the over-prediction of  $NO_x$  values.

### 3.4 Reaction path analysis

Additionally, alongside the adiabatic Free Flame calculations reaction path diagrams are generated for the elements Nitrogen, Oxygen and Carbon. These diagrams display the different reaction paths of the element with mechanism weight measures.

As a result one can observe the importance of certain formation pathways. The most prevailing path is referenced with a factor of 1.0. The other reaction ways are correlated to this reaction (with a factor naturally smaller than 1.0). Furthermore, one can specify a threshold above which species are mentioned. For the simulation this is chosen to be 0.01. Again, a few words to the file types used. *Cantera* creates the diagrams in .dot files. Dot is a file type that uses a textual description (Code) for diagrams. These files are opened with *gvedit*, a program that compiles the diagram code and offers an option to export it to a picture format (in this case .jpg). Similarly, these files can be converted using the command prompt or in python itself. For this automatic conversion environment variables corresponding to the .dot converter need to be set in the operating system. Alternatively, one can use the *dot2tex* package for \(\mathbb{T}\vec{F}\mathbb{X}\) compilation.

## 4 Results and Discussion

In this chapter the numerical results are presented and discussed. In general, two different influences on  $NO_x$  formation for water injection in the combustion chamber are detected: the physical temperature decline and a chemical influence by a change in radical concentrations.

Firstly, the setup of constant equivalence ratios is treated. Naturally, one obtains a strong decrease in flame temperatures for increasing water-to-fuel ratios  $\Omega$ . The impact of water injection on  $NO_x$  formation is considerably high. However, high mixture temperatures are desired in gas turbines in order to attain high performances and efficiencies.

Secondly, also a scenario of constant flame temperatures is investigated as described in chapter 3. The equivalence ratio is adjusted for varying water injection in order to reach the same flame temperature.  $NO_x$  formation depends strongly on temperature and thus, a lower impact of the water injections is found. Although the temperature remains constant in the test cases, a change in  $NO_x$  formation is observed. The reason is a different radical concentrations caused by the water. Other reaction pathways are favored and hence,  $NO_x$  emissions change for different water injection ratios.

Of course, there is a limit for water amounts. In the examination a maximum amount of  $\Omega = 1.5$  is examined. In theory much greater water proportions are feasible. An evaluation of the developed tool rounds off the presented emission values.

Thirdly, trends in the combustion chemistry are demonstrated through reaction path diagrams. In particular, radical concentrations and temperatures drive the formation mechanisms.

In a last step, experimental data is compared to the numerical results. A significant discrepancy is determined. It becomes clear that the simulation tool needs to be further improved so that it produces results similar to the experimental test facility.

### 4.1 Numerical Results - Constant Equivalence Ratio

Numerical results show that the flame temperature decreases as water is injected. At the same time  $NO_x$  values decrease as the flame temperature is reduced. The temperature drop is also the intuitive consequence since water (almost non reacting) increases the heat capacity of the mixture. Thus, the flame is cooled down. In conclusion, lower temperatures indicate a tendency towards reducing  $NO_x$  formation for this setup.

Furthermore lower equivalence ratios (lean combustion) lead to a reduction in temperature and  $NO_x$  emission. This is linked very well to theoretical knowledge on lean combustion. More surplus air is present in combustion as  $\Phi$  decreases. The excess air needs to be heated additionally and hence temperatures decrease.

These tendencies are discussed in the following with two developed prediction tools.

#### 4.1.1 Pollutant formation in the One-dimensional Free Flame

Nitrogen oxide pollutant formation strongly depends on flame temperature due to the thermal pathway of  $NO_x$  production. Reaction rate coefficients in general depend exponentially on temperature. Hence, the flame temperature indicates a tendency in the amount of  $NO_x$  emissions. Higher flame temperatures result in bigger  $NO_x$  formation rates.

#### Flame-Temperatures

A temperature profile in the One-dimensional Free flame is depicted in figure 4.1 for different equivalence ratios.

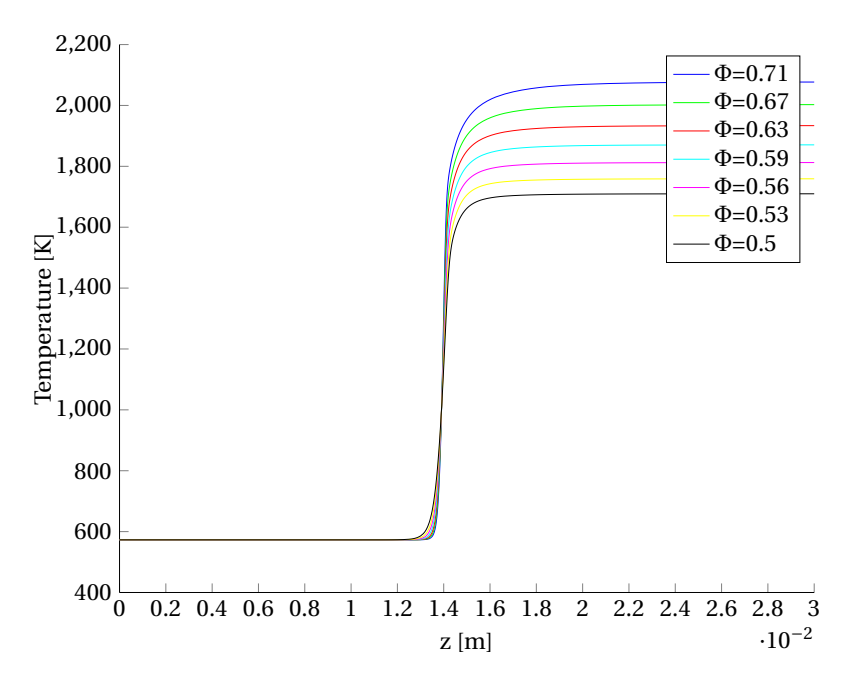


Figure 4.1: Sample temperature profile for different equivalence ratios,  $\Omega = 0$ ,  $T_{pre} = 573K$ 

One can see the typical temperature behavior of a Free Flame. At z=0 the specified species temperature occurs and reactions are occurring gradually. The temperature rises slowly until almost the center of the domain. A sudden change in temperature takes place at the location corresponding to the chemiluminescent flame front in the experiment. This region is refined automatically by *Cantera* for modeling the fast-occurring combustion reactions. The rise in temperature is a result of heat release by strong exothermic reactions. Temperature diffusion processes smoothen the profile. After the flame front, most exothermic reactions have approached an equilibrium state. Hence the temperature changes are small and at the outlet the equilibrium temperature is reached. The temperature profile is plotted for different equivalence ratios. As expected flame temperatures increase when approaching stoichiometric configurations.

Another parameter of variation in the simulation is the mass-related water-to-fuel ratio  $\Omega$ . The injected water does not influence hydrocarbon flames with exothermic reactions; hence,

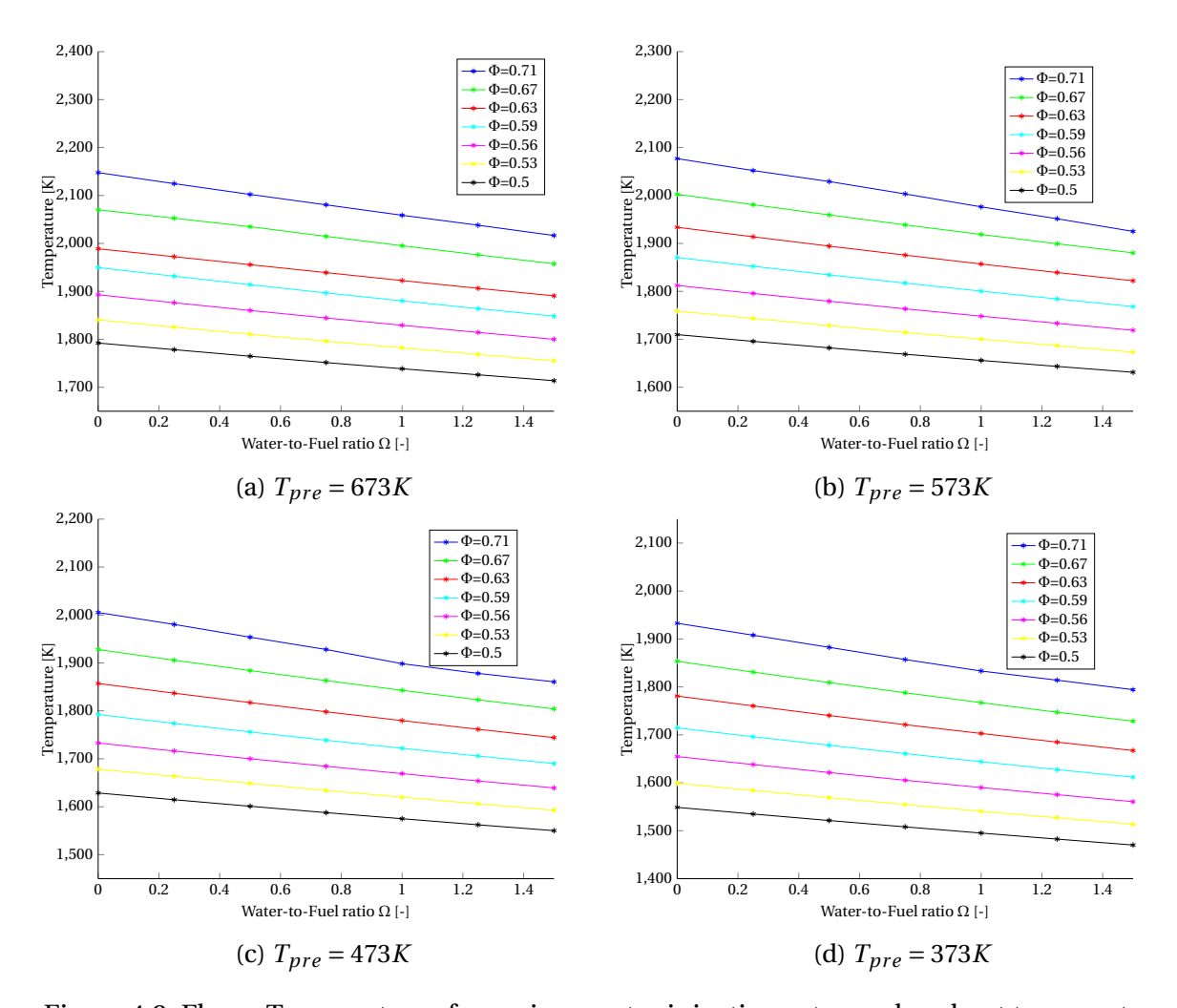


Figure 4.2: Flame Temperatures for various water injection rates and preheat temperatures

the water does not release additional heat. The theoretical explanation involves again the necessity of heating a supplementary, non-reactant species. The inert water needs to be additionally heated by the heat release of the combustion. As a result the flame and the exhaust gas reaches lower temperatures. In the case of varying lean combustion also a decrease in temperature is observed for decreasing  $\Phi$ . In the lean combustion case the inert species is excess air; for water injections the inert species is water.

The results are shown in the graphs 4.2 for different preheat temperatures. Various effects can be seen which are described in the following.

First of all, a linear temperature decline with approximately equivalent slopes is observed for all measurement series. These trends reveal that water has a similar effect on temperature in all investigated regimes. Also, the flame temperature plots can serve as a first data revision. No unphysical measurement point appears in the calculated data. Nevertheless, all measurement points are depicted to show that no unexpected effect is occurring.

Secondly, the difference in preheat temperature  $\Delta T_{pre}$  results not consequentially in the same  $\Delta T$  in flame temperatures. This effect is due to the temperature dependence of heat capacity.

For example, the setup of  $T_{pre} = 673K$ ,  $\Phi = 0.71$  and  $\Omega = 0.00$  reaches an adiabatic flame temperature of  $\sim 2150K$ . The same setup for a preheat temperature of 373K attains only a flame temperature of  $\sim 1920K$ . Therefore, in this particular case a difference of  $\Delta T_{pre} = 300K$  leads only to change in flame temperate  $\Delta T_{flame}$  of 230K.

#### **Nitrogen Oxide Emissions**

The main task of the simulations is the prediction of  $NO_x$  pollutant formation in the combustion chamber. The One-dimensional Free Flame calculates species concentrations at each grid point. A profile of the nitrogen oxide concentrations in the computational domain of the Free Flame is plotted in figure 4.3 for different water injections. The same behaviour can be observed at all measurement points.

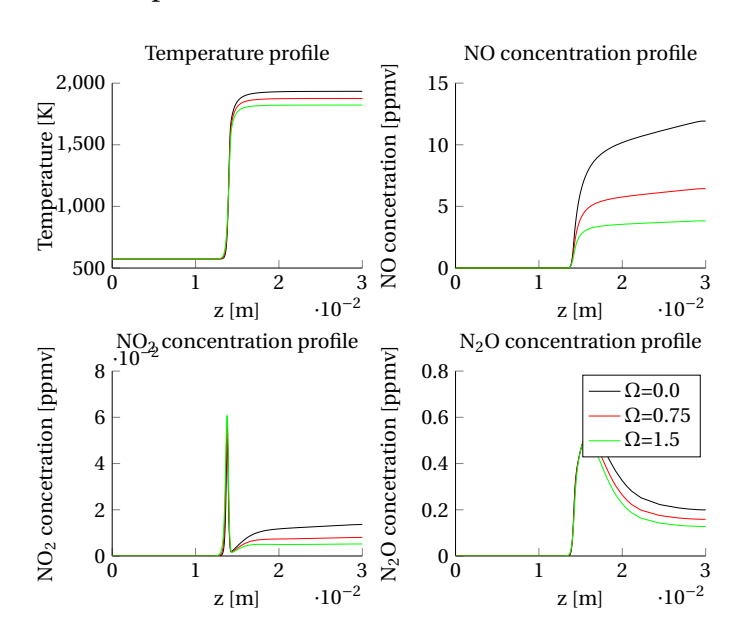


Figure 4.3: Typical profile for temperature and Nitrogen oxides,  $T_{pre} = 573K$ ,  $\Phi = 0.625$ 

Low temperatures from the inlet until roughly 0.013 m induce slow reactions and negligible Nitric oxide values. At the flame front (thickness of  $\sim$ 1 mm) a clear jump of temperature and concentrations occurs.

*NO* concentrations rise abruptly in the flame front. As stated in 2.2.1, the formation rate by the Zel'dovich/thermal pathway is increased in the flame front because of a high atomic oxygen concentration (Superequilibrium conditions). Furthermore, intermediate species in the flame front result in high prompt mechanism formation rates (see 2.2.2). Also, the *NNH* mechanism is present in the flame front. An investigation of predominate reaction mechanisms is performed in section 4.4.

Additionally, a linear growth of NO values can be observed in the post-flame zone. The thermal mechanism has not reached an equilibrium state in the Free Flame domain. Higher flame temperatures occur for smaller  $\Omega$ . Also, steeper slopes of the concentration appear for smaller  $\Omega$ . This effect is caused by the temperature dependency of the thermal pathway.

The profile for  $NO_2$  shows an impulse behavior because of high radical concentrations in the flame front. However, by comparing the scales one notices that  $NO_2$  values ranges in orders of  $10^{-3}$  less than NO values. Therefore,  $NO_x$  concentrations in the exhaust gas mainly consist of NO molecules whereas  $NO_2$  is negligible.

Furthermore, as described in the theoretical part, NO can be produced by the Nitrous Oxide ( $N_2O$ ) path.  $N_2O$  is decomposed downstream of the flame to  $N_2$  and NO. This behavior can be observed in the plot for the  $N_2O$  concentration.

Figure 4.4 shows Free Flame  $NO_x$  relative exhaust gas concentrations. Two different preheat temperatures are displayed to demonstrate the impact of preheat temperature on  $NO_x$  formation for water injection.

The last grid point of the Free Flame domain is used for exhaust concentrations. For an adjustment to the probe location the reactor network solution is developed. All values are normalized to a 15% exhaust oxygen concentration. The procedure is described in the appendix. This step is necessary to compare emission concentrations to other configurations.

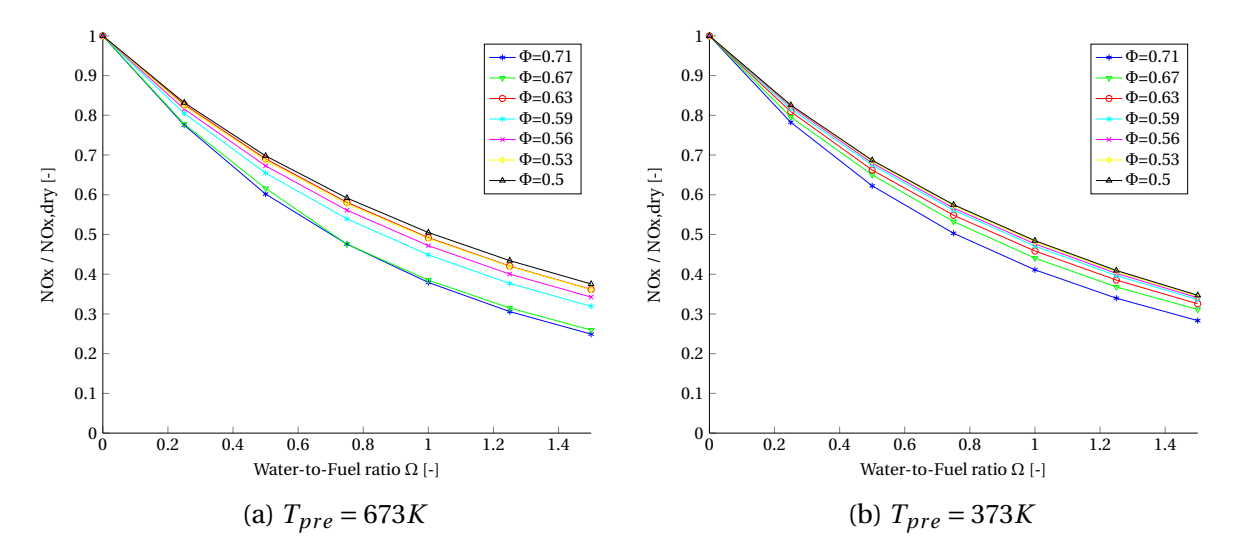


Figure 4.4: Exhaust  $NO_x$  concentrations relative to corresponding dry unburnt configuration

A significant nonlinear decline of  $NO_x$  exhaust concentrations is observed. A higher water proportion  $\Phi$  reduces the  $NO_x$  emission values for all measurement series. It can be seen that a stronger  $NO_x$  decrease for water injection occurs for bigger equivalence ratios  $\Phi$ . The measurement series of  $\Phi = 0.71$  shows a reduction of  $NO_x$  emissions up to 70%. For lower preheat temperatures smaller reductions of  $NO_x$  emissions occur for water injection. Furthermore, at lower preheat temperatures the measurement series for various equivalence ratios show smaller differences in the trends.

One can conclude that the flame temperature has a significant impact on the tendency for  $NO_x$  production. A decrease in flame temperature and in  $NO_x$  exhaust concentration is observed as water is injected. Figure 4.5 compares the temperature decline to the  $NO_x$  decrease relatively. The graph shows a decrease in flame temperature and  $NO_x$  formation due to water injection. For higher flame temperatures at  $\Phi = 0.71$  a bigger relative drop in flame temperature occurs. Simultaneously also a steeper decline in  $NO_x$  formation is calculated.

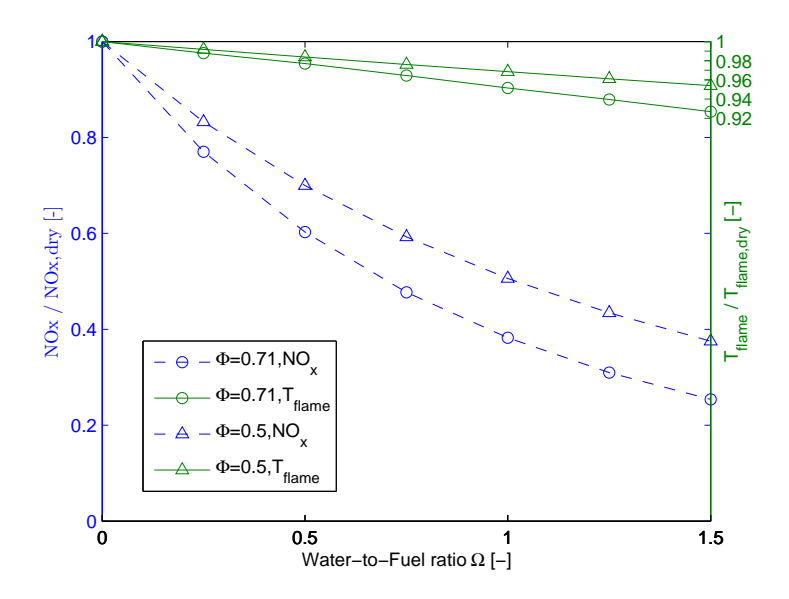


Figure 4.5: Relative  $NO_x$  emission values compared to flame temperature,  $T_{pre} = 573K$ 

In particular, one notices an interesting trend of the non-linear  $NO_x$  formation decline. Although a linear decrease in temperature is observed as water is injected (see figure 4.2), a non-linear behavior in the  $NO_x$  values arises. The non-linear decline looks similar to an exponential dependency. Assuming an Arrhenius temperature dependence the impact of water injections is exponential, as reaction rate coefficients depend exponentially on temperature. Nevertheless,  $NO_x$  formation rates also depend on other factors, especially radical concentrations as described in section 4.4.

#### 4.1.2 Pollutant formation of reactor network

To improve the accuracy of the prediction flow information is incorporated using a reactor network. The flame front is modeled by the previous Free Flame data at 95% temperature progress. Afterwards, the reactor calculates concentrations to the location where emission measurements are collected. More details on the modeling of the reactor network are explained in chapter 3.

 $NO_x$  formation rates in the post-flame zone are mainly produced by the Zel'dovich pathway. This  $NO_x$  formation path depends on the temperature and atomic oxygen concentrations. Figure 4.8 in the later section 4.2 reveals, that the temperature and atomic oxygen concentrations remain roughly constant in the post-flame zone of the computed Free Flame. Thus, similar to the NO formation behavior in the Free Flame the Nitric oxide production rate in the perfectly stirred reactor (PSR) is constant; this results in a linear  $NO_x$ -concentration growth. A sketch of the  $NO_x$  concentration in the Perfectly Stirred reactor for different residence times is depicted in figure 4.6.

The PSR uses time as a coordinate frame time instead of a spatial variable that is used in the Free Flame. The probability density distribution of the particle residence times adjusts the concentration measurements according to the probe location. A coordinate transformation

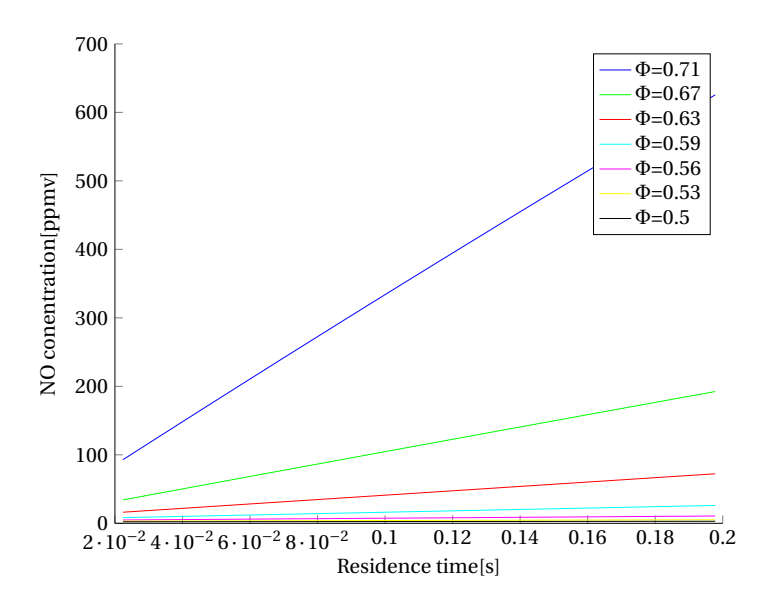


Figure 4.6: Typical profile for Nitrogen oxides concentration in a reactor,  $T_{pre} = 573K$ ,  $\Omega = 0$ 

between time and distance is linear if the axial flow velocity is constant.

$$v = \frac{s}{t} \approx const. \Longrightarrow s \propto t$$

Hence, a linear growth in distance for the Free Flame will also lead to a linear increase in time for the reactor. The influence of mixture temperatures is analogous to the One-dimensional Free Flame scenario  $NO_x$  formation.

Higher  $NO_x$  concentrations in the reactor for bigger equivalence ratios  $\Phi$  have mainly two reasons: a bigger initial  $NO_x$  concentrations and higher temperatures.

Firstly, a higher preheat temperature, a higher  $\Phi$  or a lower  $\Omega$  leads to higher flame temperatures. In the case of a higher flame temperature, the reactor is initialized with a bigger concentration of  $NO_x$ . For illustration one can compare figure 4.3 at a distance value of  $\sim 16mm$  for different  $\Phi$ . The NO value is an acceptable estimate due to the fact that it covers more than 90% of  $NO_x$  concentrations.

Secondly, the reactor is initialized with a higher temperature since the reactor initial temperature is always 95% of the equilibrium temperature. As a consequence one observes different slopes ( $NO_x$  production rates) and values in figure 4.6.

The reactor network approach is applied to each test case. The absoulute emission results are presented in figure 4.7. The strong influence of temperature in  $NO_x$  formation becomes clear by comparing the different preheat temperatures. Correa suggests that a flame temperature reduction of 90 K results in a 50% reduction of  $NO_x$  production rates [4]. However, for the numerical measurements a slightly stronger  $NO_x$  reduction due to flame temperature decline. Therefore, the dry  $NO_x$  emissions values are compared for different preheat temperatures. A difference  $\Delta T_{pre} = 100K$  leads to a decline in flame temperature of roughly  $\Delta T_{flame} = 90K$  (see section 4.1.1 and figure 4.2). Nevertheless, a reduction factor of about three in  $NO_x$  emission values is found. Hence, in the numerical results a greater temperature dependency of  $NO_x$  formation is observed than the estimation of Correa.

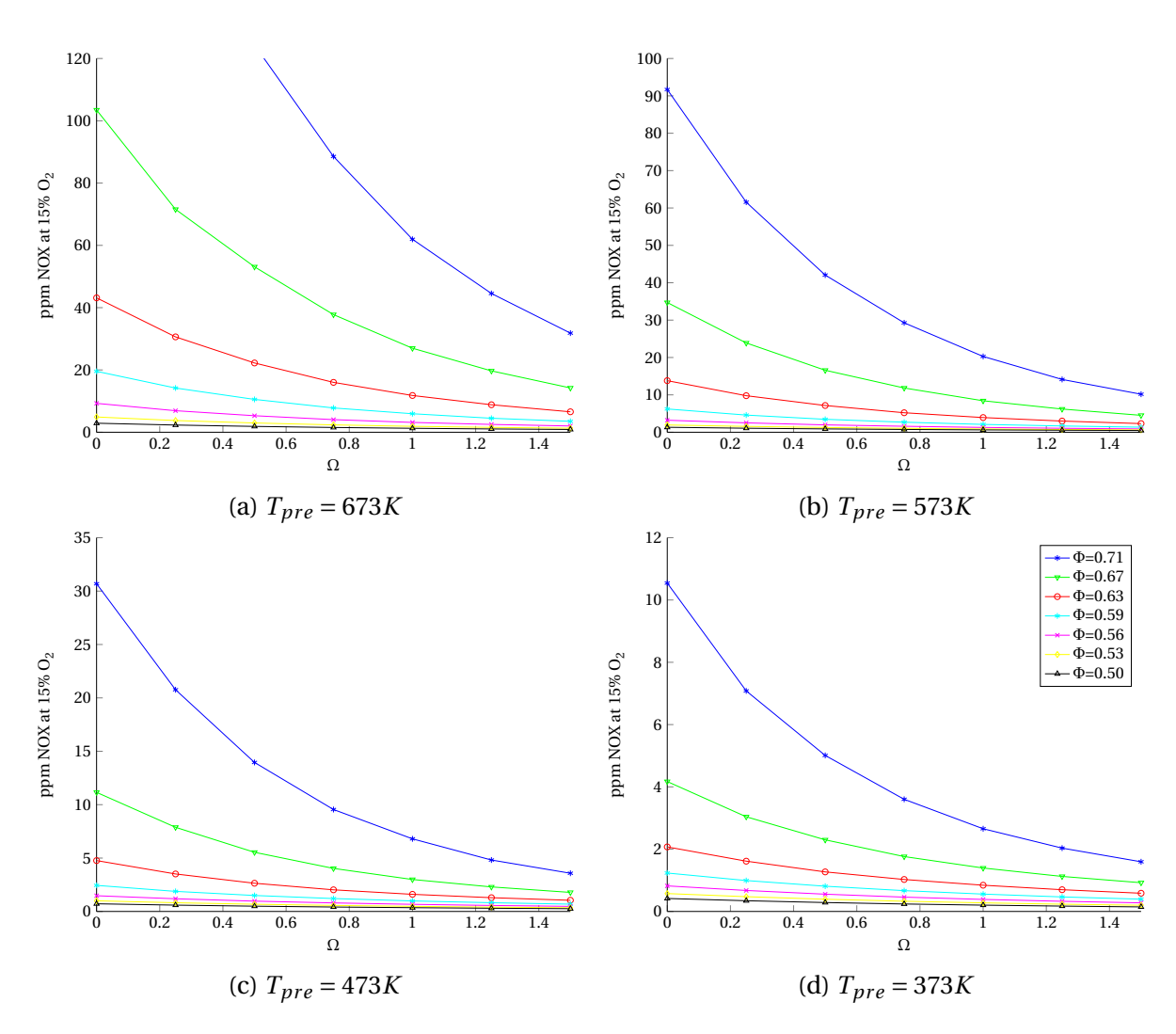


Figure 4.7: Exhaust  $NO_x$  concentrations calculated by the reactor network

The absolute value of  $NO_x$  emission concentrations is discussed in the following paragraph. Especially the graph corresponding to a preheat temperature of 673K reveals that  $NO_x$  values are particularly high. Reasons are the absence of heat transfer in numerical calculations. Computed temperatures of more than 2100K occur which leads to high formation rates. At such high temperatures the heat loss has a significant impact on  $NO_x$  formation rates, particularly through the thermal pathway. These high temperatures result not only in an overprediction in reaction coefficients, but also in overestimation of atomic oxygen O concentrations (see 2.2.1). As a consequence, the tool computes unphysical emission values of roughly 200 parts per million volumetric (ppmv)  $NO_x$ . An exemplary incorporation of heat removal corrects these simplifications and is discussed later in section 4.5. However, this is just an outlook with suitable heat transfer coefficients. Future work needs to focus on estimating this heat removal.

Disregarding the fact of over-predicted values one can see the trend in  $NO_x$  formation due to water injections. In particular the fuel richer cases show a drastic absolute decline because of higher flame temperatures. The low preheat temperature of 373K (100°C) show favorable conditions as they lead to  $NO_x$  emission concentrations of less than 1ppmv. In all cases one can observe that a water injection positively influences  $NO_x$  reduction (see figure 4.4). Nevertheless, exhaust temperatures and thus the gas turbine performance and efficiency is decreasing.

## 4.2 Numerical Results - Constant Flame Temperature

The question is raised whether the previously described  $NO_x$  reductions are solely due to the temperature decrease. To investigate this concern the combustion temperature is kept constant. In order to provide the additional heating energy for the injected water the equivalence ratio  $\Phi$  is increased. The desired flame temperature is always similar to the dry case flame temperature  $T_{flame,dry}$ .

#### 4.2.1 Pollutant formation of One-dimensional Free Flame

Temperature profiles in Free flames are discussed in section 4.1.1. In the scenario of constant flame temperatures the same temperature profiles are obtained for increasing  $\Omega$ .

#### **Radical concentration**

Since temperatures are constant other reasons for changes in  $NO_x$  formation rates need to be discussed.  $NO_x$  reaction paths are significantly influenced by radical concentrations; radicals show peak concentrations at the location corresponding to the flame front. A typical Free Flame concentration profile for atomic hydrogen H, atomic oxygen O and hydroxyl OH is depicted in figure 4.8. At this point just an abstracted view on radical concentrations is given. Section 4.4 points out more detailed investigations.

The temperature profile with varying  $\Omega$  remains equivalent. H, O and OH concentrations generally show a peak at the flame front because of many different reactions. The O concen-

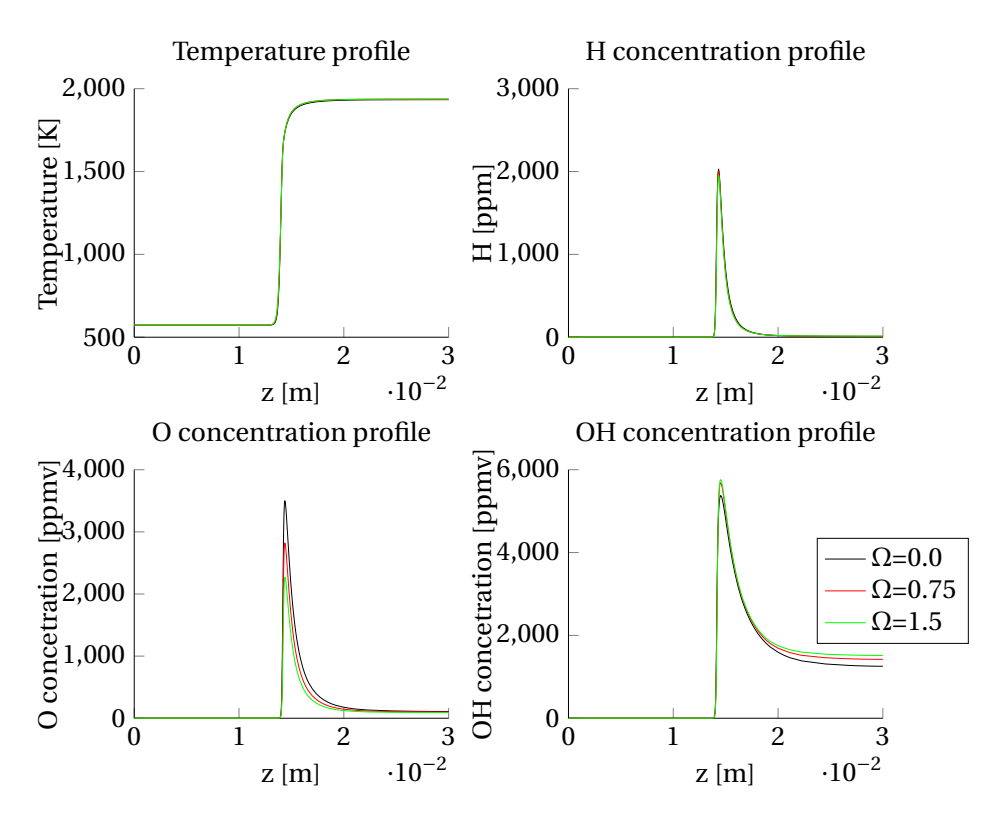


Figure 4.8: Typical profile for radical concentrations over distance,  $T_{pre} = 573K$ ,  $\Phi = 0.63$ 

tration is reduced as  $\Omega$  increases. No significant changes are seen in the atomic hydrogen H values for water injection.

The thermal pathway of  $NO_x$  formation is directly driven by atomic oxygen concentrations. The graphs clearly show continuously higher concentrations in cases of smaller  $\Omega$ . Thus, although the temperature remains the same, lower thermal  $NO_x$  reaction rates are obtained for higher water-to-fuel ratios  $\Omega$ . Nevertheless, wet initial compositions induce slightly bigger hydroxy radical (OH) concentrations.

#### **Nitrogen Oxide emissions**

In general,  $NO_x$  concentrations decrease for an increasing water injection rate in Free Flame calculations also at constant flame temperature. Of course, the impact of water injection is clearly smaller since  $NO_x$  formation mechanisms are significantly temperature-driven. Nevertheless, the water injection has an impact on the combustion chemistry due to radical changes. The characteristic behavior of nitrogen oxides along the One-dimensional Free Flame spatial coordinate z is depicted in figure 4.9.

Similarly to the constant equilibrium ratio case  $NO_x$  values show a large increase at the flame front. Although the temperature remains constant for varying  $\Omega$ , the nitrogen oxide concentrations are consistently reduced in wet compositions.

Lower values in the *NO* concentration profile are due to a reduced concentration of *O* radicals. The *NO* formation through the thermal path depends directly on *O* concentrations. The linear increase of *NO* concentrations in the post-flame is produced by the thermal pathway.

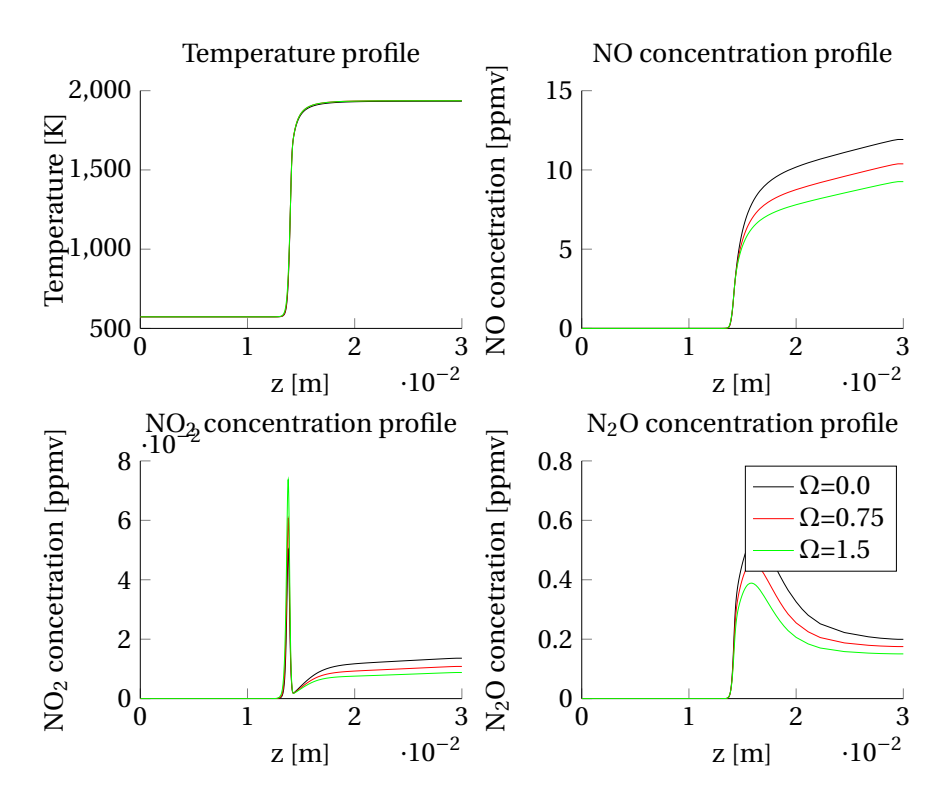


Figure 4.9: Typical profile for Nitrogen oxides concentration over distance in a Free Flame,  $T_{pre} = 573K, \Phi = 0.63$ 

Lower  $NO_x$  formation rates are not influenced by the temperature dependence but are caused by smaller radical concentrations. The  $NO_2$  profile shows increased intermediate but lower exhaust concentrations for growing  $\Omega$ .  $N_2O$  concentrations in the Free Flame are strictly decreased in wet inlet configurations. However, one needs to recall that  $N_2O$  does not contribute to Nitrogen oxides. Still,  $N_2O$  is decomposed to NO downstream.

The previously described trends in the Free Flame domain are similar for all measurement points. A summary of the  $NO_x$  exhaust gas results is displayed in figure 4.10. showing the relative changes in  $NO_x$  emissions. Compared to the constant equilibrium ration  $\Phi$  case the impact of the water injection is clearly smaller. Nevertheless trends can be observed that are discussed in the following.

Compared to the case of decreasing temperature the effect of  $NO_x$  reduction due to water injection is significantly reduced; still approximately 35% nitrogen oxide molecules in the exhaust gas can be avoided related to the dry configuration. However, the impact varies considering different equivalence ratios. Contrary to the scenario of constant equilibrium ratio in this case greater relative changes are detected for lower equivalence ratios. This seems very odd because higher temperatures occur for fuel-richer conditions and therefore greater absolute  $NO_x$  formation rates. One would naively expect that the effect of water addition is more significant for higher temperatures. However, the opposite event is observed.

Besides, the decline in  $NO_x$  concentration is roughly linear whereas an exponential decay is found in the scenario of decreasing temperatures. The exponential characteristic is a result of the Arrhenius temperature dependence of rate coefficients; in this case temperature stays

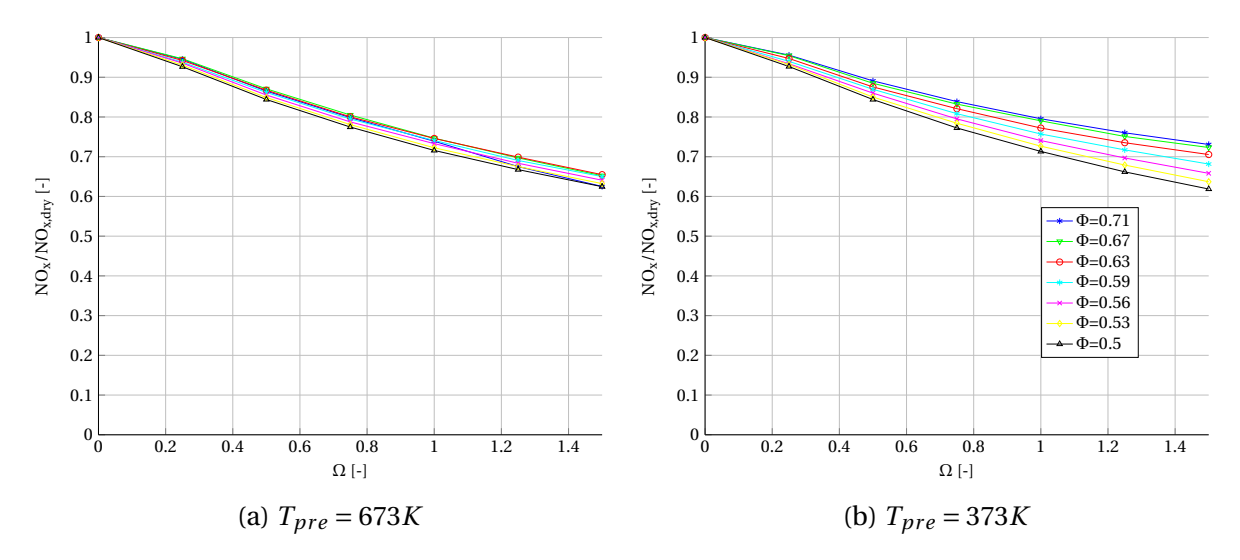


Figure 4.10: Free flame  $NO_x$  exhaust concentrations relative to dry configuration- constant flame temperature

constant and thus rate coefficients remain unchanged. Single species concentrations affect the formation rate linearly (in bimolecular reactions). The radical concentrations seem to be the main driver for the changes in  $NO_x$  values.

Another very interesting aspect is the discrepancy in the graphs for different preheat temperatures. At lower preheat temperatures the trends for various  $\Phi$  differ more evidently than in hot preheated scenarios. For the low equivalence ratio  $\Phi$  of 0.5 the plots show almost no difference for varying  $T_{pre}$ . At fuel-richer conditions the  $NO_x$  reduction effect loses significance for lower preheat values. For example, at  $T_{pre}$  = 673K and  $\Phi$  = 0.71 a reduction in  $NO_x$  emissions of nearly 35% is calculated for  $\Omega$  = 1.5; the same scenario at  $T_{pre}$  = 373K results only in a 25% nitrogen oxide decline.

In conclusion, scenarios of increasing  $\Phi$  approach to the stoichiometric configurations and lead to high temperatures. The absolute  $NO_x$  exhaust concentrations are higher for increased flame temperatures. Nevertheless, a smaller relative  $NO_x$  reduction factor is obtained for higher flame temperatures.

#### 4.2.2 Pollutant formation of reactor network

Numerical  $NO_x$  values calculated by the reactor network are also decreasing for rising  $\Omega$  and constant flame temperatures. Therefore the  $NO_x$  changes are not only a result of the temperature decrease by water injections. The injection of water has a positive effect on  $NO_x$  pollutant formation. Numerically calculated emission concentrations at the probe location are illustrated in figure 4.11.

Analogous to the relative results calculated by the Free Flame also an approximate linear decline in  $NO_x$  concentrations is calculated by the reactor network. This is similarly due to the fact that the reaction rate coefficient remains the same and formation rates depend solely on radical concentrations.

A literature review or a peek into section 4.5 reveals that the presented absolute  $NO_x$  emis-

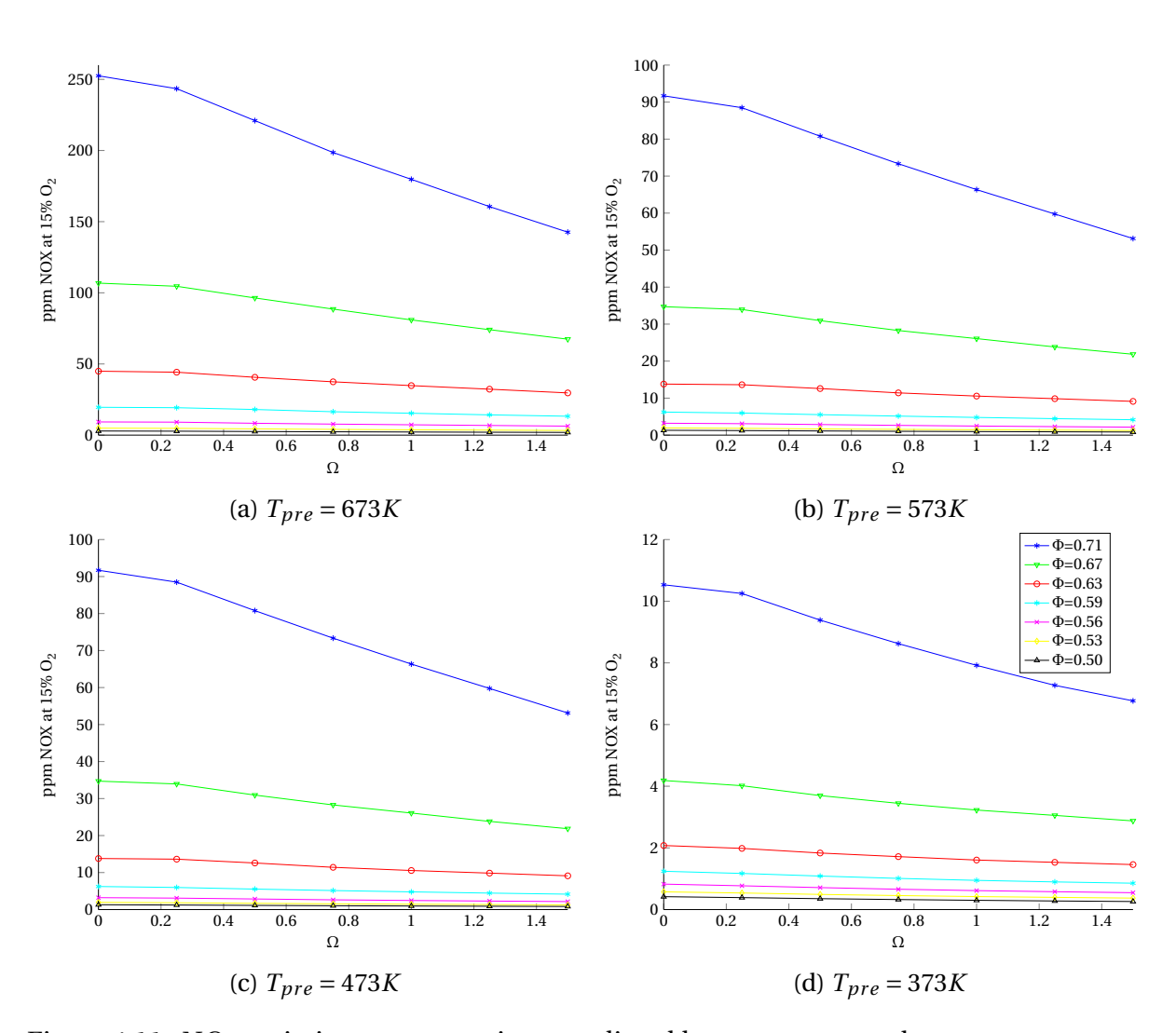


Figure 4.11:  $NO_x$  emission concentrations predicted by reactor network at constant temperature

sion values are unusually high. This is because the reactor network assumes adiabatic conditions whereas experiments always involve heat loss. As a result the experimental temperatures are lower than numerical and as a result,  $NO_x$  formation rates are smaller.

In general,  $NO_x$  values fall for lower preheat temperatures because the flame temperature is also decreasing. The temperature dependence of  $NO_x$  formation is particularly responsible for lower concentrations at decreased equivalence ratios. Naturally higher  $NO_x$  concentrations occur for increasing preheat temperatures.

The flame temperature of the case  $T_{Pre}=373K$ ,  $\Phi=0.71$  and  $T_{Pre}=473K$ ,  $\Phi=0.67$  both roughly equal 1940K. As an interesting fact almost the same  $NO_x$  emission concentration is obtained. The same comparison can be performed for scenarios  $T_{Pre}=373K$ ,  $\Phi=0.71$  and  $T_{Pre}=573K$ ,  $\Phi=0.63$  or plenty other cases. Equal temperatures result in approximately equivalent  $NO_x$  concentrations. As stated in section 2.2.1, radical concentrations also depend highly on temperature. This means that for dry combustion  $NO_x$  formation relies strongly on temperature. Reaction coefficients, radical concentrations and as a conclusion reaction paths are similar if flame temperatures are equal for dry configurations.

However, for varying water injection rates the flame temperature is not an indicator of  $NO_x$  formation. At all points of measurement rising water-to-fuel ratio  $\Omega$  has a beneficiary effect on  $NO_x$  pollutant formation, although the temperature remains constant. These phenomenons are a consequence of the radical changes for water addition. Further influences of water in the combustion chemistry are examined in section 4.4.

In conclusion, the reactor network demonstrates detailed trends of the combustion chemistry for water addition.

## 4.3 Limitations of developed reactor network

Nevertheless, the assumptions of a perfectly mixed gaseous mixture and neglecting heat loss need to be reviewed as well as further improvements done. The numerical case of a certain preheat temperature corresponds for example to a higher value in experiment because of the vaporization enthalpy. Lower temperatures at the combustion chamber inlet occur in the experiment compared to the assumed numerical preheat temperature. Furthermore, for the case of constant flame temperature different equivalence ratios are calculated. All these concerns are summarized and discussed in the next section.

## 4.3.1 Discussion of simplifying assumptions

The developed reactor network simplifies the experimental test rig to a very abstracted model. Any information about the geometry is incorporated by particle residence times in the combustion chamber after passing an approximate flame surface.  $NO_x$  formation strongly depends on temperature and residence time and thus, this numerical setup was chosen. However, the question is discussed whether this simplified view is sufficient in predicting  $NO_x$  values.

As also mentioned in the result descriptions, the tool constantly over-predicts temperature and thus  $NO_x$  formation. Firstly, this is due to the over-prediction of the combustion chamber inlet temperature. The necessity of vaporizing the liquid water in the experiment

cools down the unburnt fuel mixture. Secondly, the calculations are performed in an adiabatic setup. In the test facility a significant heat transfer to the surroundings takes place that reduces temperatures in the combustion chamber.

#### Homogeneous mixture prior to combustion

As described in the 'Methodology' chapter *Cantera* can only handle one phase mixtures. In the experimental test rig the condition of a gaseous mixture prior to combustion is desired. Therefore, the water is injected in a way that it forms small droplets. Hereby, a small amount of atomizing air is additionally injected. Smaller droplets are essential for a fast vaporization. For the numerical tool, it is assumed that the injected water is fully vaporized prior to the flame front.

Also, for comparison of numerical and experimental setup a correction of equivalence ratios is required. Small amounts of atomizing air (5%) change the experimental equivalence ratio. The numerical equivalence ratio  $\Phi$  of 0.5 corresponds to an experimental equivalence ratio of roughly 0.494.

The ideally premixed assumption might not be 100% correct, but desired in the physical experiment. However,  $NO_x$  is also produced by regions of locally unmixed species. The fuel and water injection strategy is designed such that it prevents this  $NO_x$  formation route. This effect is disregarded in numerical computations as perfectly mixed conditions are acquired.

#### Over-estimated temperature prior to combustion

The inlet air is heated to a certain value. Regarding the  $\Omega=0$  configuration, the fuel-air mixture attains the corresponding preheat temperature downstream of a mixer after fuel injection.

Furthermore, in order to correlate the wet numerical data to the experiments one needs to consider the different setups. In the experiment liquid water is injected whereas in the numerical model steam is used. The temperature prior to combustion is therefore decreased in the experimental case by the vaporization enthalpy.

However, a further decline in flame temperature (by vaporization enthalpy) results only in the scenario of constant equivalence ratios. The injected water needs to be vaporized which lowers the combustion chamber inlet temperature and as a result, the flame temperature is further decreased in the experiment. An estimation of this unburned state is very vague due to temperature diffusion processes and necessary assumptions. An experimental temperature measurement at the combustion chamber inlet would improve the numerically assumed initial temperatures.

In the case of keeping flame temperatures constant, the concern of the vaporization enthalpy loses significance. Equal temperatures corresponding to the dry case are achieved through a variation of the equivalence ratio. Therefore, in both setups almost the same temperature is attained. Nevertheless, the numerical model still differs from the experiment. For determining the equivalence ratio for constant temperature of the experimental apparatus, the vaporization enthalpy is taken into account. In the numerical case, the water is assumed to be gaseous at the air preheat temperature. As a result, smaller equivalence ratios are calculated in the numerical setup.

Again, the most accurate solution would be a temperature measurement at the combustion chamber inlet. Using this data, one could better reconstruct the experimental scenario numerically. As described in the 'Methodology' chapter, this raises many difficulties. Currently, these assumptions are made since a better estimation is very vague.

#### Heat removal by combustion chamber cooling

The experimental test apparatus contains several cooling mechanisms (see section 3.1.4 and figure 3.1). The calculations are performed adiabatically on the contrary to heat loss in test apparatus. Therefore, higher temperatures occur especially in the post flame zones; hence, this results in higher  $NO_x$  formation rates. In the following, the influence of several forms of heat removal is described.

In a first step radiative heat transfer through the fused silica walls in the combustion chamber is examined. In reality, flame fronts are cooled by emitting heat radiation to the environment. Radiative heat transfer occurs in the test apparatus to the water-cooled combustion chamber walls or to the environment through the fused silica walls. In order to improve the accuracy of the numerical tool an estimation of this heat loss would be useful. In the numerical model the adiabatic assumption in the flame front over-predicts the  $NO_x$  formation. However, a rough approximation of the decline in flame temperature by radiative emission is very vague. Therefore, the amount of  $NO_x$  over-prediction cannot be determined.

In a second step the water cooling mechanism of the combustion chamber is studied.  $NO_x$  molecules produced in the post flame zone are mainly formed by the thermal path. Since this process significantly depends on temperature, a more detailed analysis regarding the impact of combustion chamber water cooling is necessary.

Post-flame temperatures of more than 1500K are reached in the test facility. Cooling water flows through the combustion chamber walls. At the outlet the pumped water has a temperature of less than 310K. Thus, a great temperature difference occurs between the gas flow inside the burner and the walls. One needs to develop a model for the heat transfer between a cool wall and hot flowing gas. In section 4.5 a heat transfer coefficient fitted to experiments is used.

#### 4.3.2 Discussion of developed reactor network approach

Two main reactive zones are identified in the combustion setup: the flame front and the post-flame zone. The numerical simulation approach involves a Free Flame and a reactor network. The Free Flame models complex reaction processes in the flame front. A reactor network models the post-flame zone. For the post-flame region a probability distribution of particle residence times in the combustion chamber was utilized for the reactor network.

A Free Flame modeling is used because of two reasons. Firstly, regardless of where the particles cross the flame front, approximately the same reactions are occurring. Secondly, the flame front is very thin. Any particles crossing the flame surface can be interpreted as One-dimensional. Thus, the One-dimensional Free Flame calculation serves as a good estimate of concentrations shortly after the flame front. This point is set directly behind the Flame Front, where the temperature has reached 95% of the adiabatic flame temperature.

The idea of a preceding reactor network was sparked by the fact that post-flame  $NO_x$  strongly depends on residence time. Additionally, the strong swirl mixes the exhaust gas in

a way so that a homogeneous mixture is attained. As a consequence a perfectly stirred reactor is deemed to be an appropriate model. Residence times are incorporated using a probability density approach.

This methodology seems to be very promising in the prediction of  $NO_x$  species. However, many other combustion rig simulations use a zonal modeling for the reactor network (E.g. Fichet [7] or Falcitelli [6]). For producing prompt and reliable output Free Flame simulations demand too much computational power. Furthermore, Free Flame calculations often face convergence issues. At many measurement points the simulation had to be restarted due to time integration failure. In contrast the reactor network is stable at every configuration.

For these reasons the developed model is not suitable for industry usage. Nevertheless, the tool serves well for a fundamental parameter study as performed in the course of this thesis.

## 4.4 Reaction Path analysis

The purpose of this section is the explanation of observed  $NO_x$  reduction trends for water injection.

As mentioned in the scenario of constant equivalence ratio, temperature affects the  $NO_x$  formation strongly. On the one hand reaction rate coefficients are influenced. On the other hand radical concentrations depend highly on temperature. In the case of constant temperature radical concentrations are influenced by water.

In the following formation paths and trends in the radical concentrations are discussed.

#### 4.4.1 Radical concentrations

In order that reactions occur all  $NO_x$  formation mechanisms require the presence of radicals. Generally, a peak in radical concentrations appears in the flame front. The behavior of such reactive species in the course of a One-dimensional Free Flame is examined for different water injection ratios.

#### **Constant Equivalence Ratio**

In this section the setup of constant equivalence ratios is examined. Hence, the effects are dominantly caused by the physical effect of the temperature drop. Flame temperatures drop for higher water-to-fuel ratios  $\Omega$ . This discrepancy in temperature affects the reaction rate coefficients and radical concentrations. Figure 4.12 shows the typical effect of rising  $\Omega$  on O concentrations.

Obviously, a sharp peak appears at the location of the flame front. The height of this peak decreases as more water is injected. First, the decline in temperature is responsible for this change. Secondly, injected water influences radical concentration, and as a consequence, atomic oxygen concentrations fall.

The atomic oxygen concentration has a high influence on  $NO_x$  formation. For instance the thermal path requires in the rate determining step  $N_2 + O \rightarrow NO + N$  an oxygen radical. At drier conditions the atomic oxygen concentration is increased and thus, a greater  $NO_x$  formation rate is observed. Furthermore, in this case the temperature is a leading factor.  $NO_x$ 

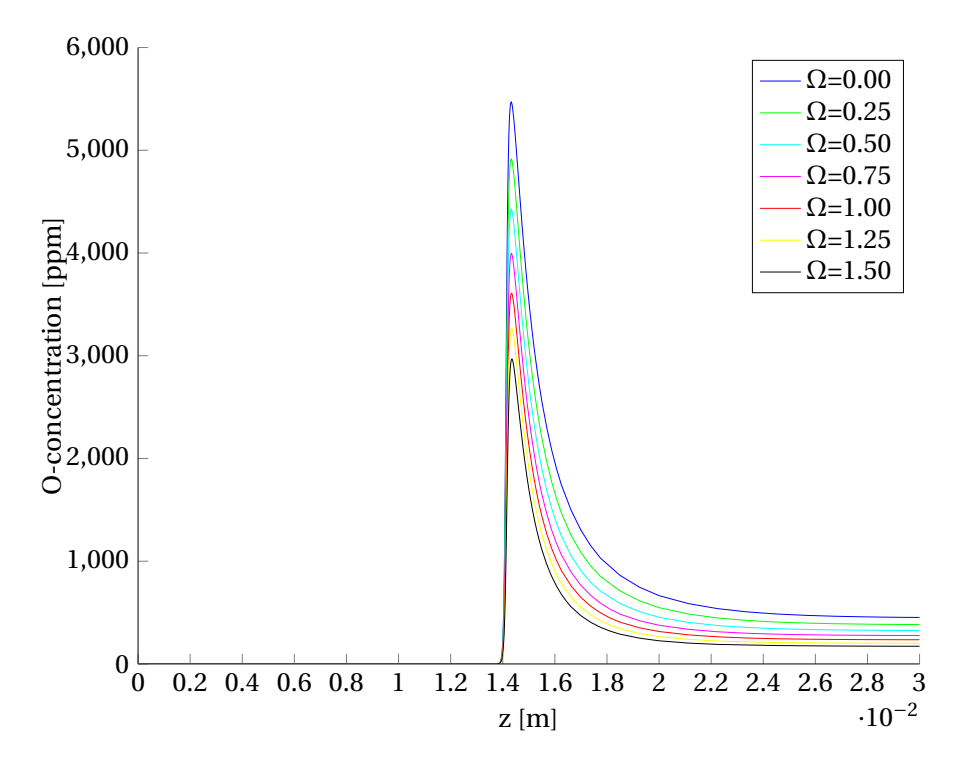


Figure 4.12: Typical profile for atomic oxygen concentrations,  $T_{pre} = 673K$ ,  $\Omega = 0$ 

formation reaction coefficients also decrease which induces an even further decline of  $NO_x$  concentration at wet conditions.

For a more detailed study of the radical changes, peak atomic oxygen concentrations are plotted in figure 4.13 alongside the flame temperature. These atomic oxygen peaks occur at the location of the flame front, similar to the typical concentration profile given in figure 4.12. In general, a greater value for the maximum atomic oxygen concentration results also in higher *O* concentrations in the post-flame zone. On the other axis the flame temperature decline is plotted.

One can see decreasing trends with water injection similar to the temperature and  $NO_x$  formation decline. However, when comparing it to figure 4.4 it becomes clear that  $NO_x$  values fall more significantly than radical concentrations. The reason is simply that also reaction rate coefficients are influenced by temperature. Besides, temperature decreases linearly as injected water is increased. Radical concentrations decline stronger than the temperature. At higher  $\Phi$  radical concentrations are increased due to higher flame temperatures.

In the flame front also the prompt mechanism of  $NO_x$  formation is important. Intermediate species in the flame front, such as CH or  $CH_2$  radicals, are responsible for decomposing atmospheric nitrogen. The plots in figure 4.14 depict the sharp peak in CH and  $CH_2$  concentrations in the flame front. These species are very reactive and only occur in the flame front. Therefore, only the profile corresponding to the flame front is plotted. At other locations the CH and  $CH_2$  concentrations are negligibly small.

One can observe that radical concentrations fall when injecting higher proportions of water. Both CH and  $CH_2$  concentrations are reduced at wet inlet conditions. Nevertheless, one can also notice that peak radical concentrations of both species are two orders lower than

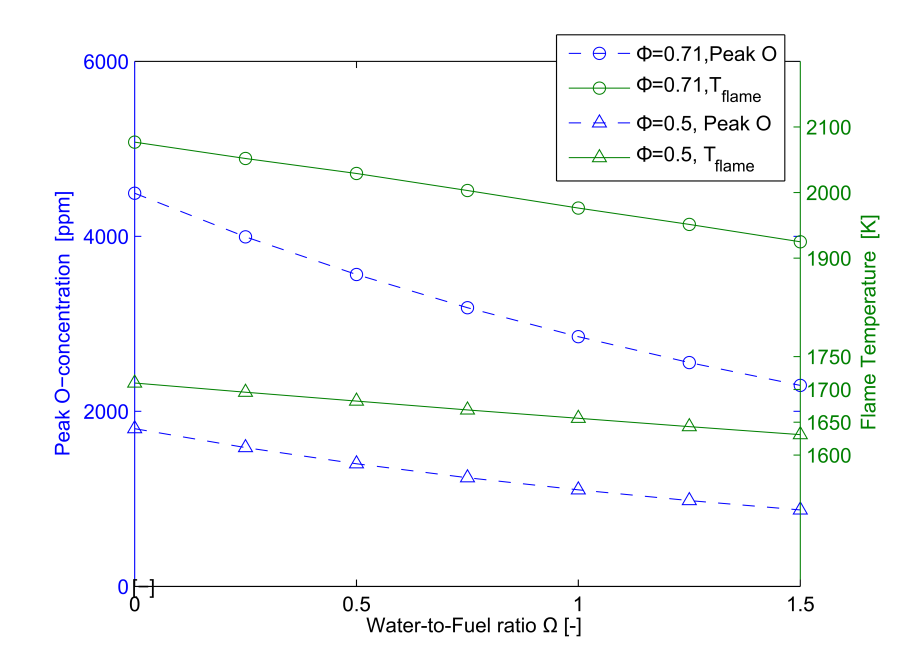


Figure 4.13: Peak atomic Oxygen O concentrations and flame temperature - constant equivalence ratio,  $T_{pre} = 573 K$ 

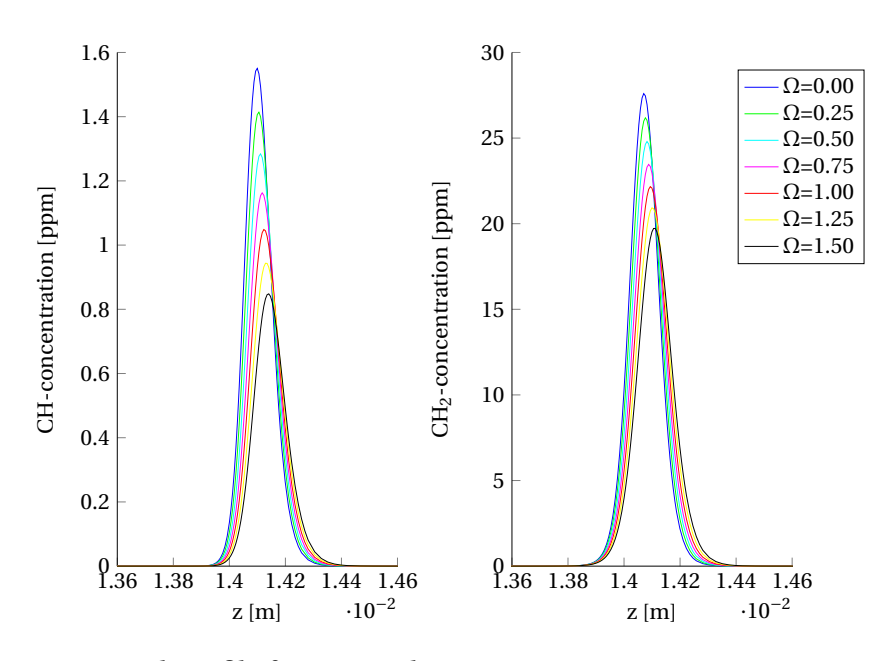


Figure 4.14: Typical profile for CH and  $CH_2$  concentrations,  $T_{pre}=673K, \Phi=0.71$ 

atomic oxygen concentrations. As stated in the theoretical part,  $NO_x$  formation rates through the prompt mechanism are more significant in fuel-richer regimes ( $\Phi > 0.8$ ). Thus, the highest observed equivalence ratio is plotted. At lower equivalence ratios these radical concentrations are reduced.

#### **Constant Temperature**

In the previous section the scenario of constant equivalence ratios was examined. The decline in radical concentrations is not solely led by the temperature drop. In this section the chemical impact of water injection is investigated. Also at constant flame temperatures peak oxygen and nitrogen oxide concentrations decrease as more water is injected. The results are presented in figure 4.15. Of course, relative changes are smaller when keeping the flame temperature constant.

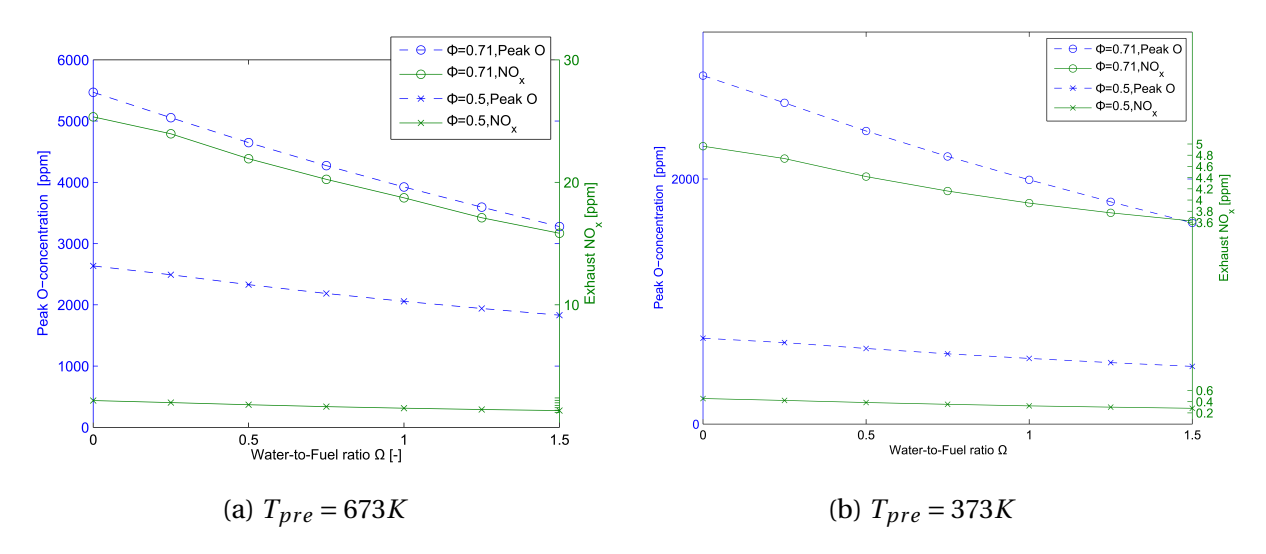


Figure 4.15: Peak atomic Oxygen O concentrations and  $NO_x$  concentrations at constant temperature

In fact, higher preheat temperatures result in increased flame temperatures. Due to the temperature dependence higher peak oxygen and nitrogen oxide concentrations occur (compare scales). Additionally, at rising  $\Phi$  flame temperatures are increased and hence, radical and  $NO_x$  concentrations rise.

At fuel-richer conditions ( $\Phi = 0.71$ ) a more significant decline in peak atomic oxygen concentrations is obtained. In this regime higher flame temperatures occur and the decline in  $NO_x$  and oxygen radicals is stronger.

The decrease in  $NO_x$  values can well be compared to the observed atomic oxygen trend. One can conclude an approximately proportional dependence between radical concentration and  $NO_x$  formation rate. This is also the theoretical expectation, since bimolecular reactions depend linearly on their reactant concentrations. Most formation reactions are bimolecular. Nevertheless, the flame temperature in the different measurement series changes the reaction rate coefficient; hence different slopes and dependencies of the  $NO_x$  decline appear in the diagram.

#### 4.4.2 Reaction path diagrams

The following section demonstrates the impact of water injection on nitrogen oxide reaction paths.

First, trends for different reaction mechanisms are shown for various points in the Free Flame. Depending on the flame zone certain reaction mechanisms are dominant in the formation of Nitrogen Oxides. Secondly, the impact of water on reaction paths is examined in the post-flame zone. On the one hand, the physical effect of flame temperature on  $NO_x$  formation paths is studied. On the other hand, the impact of water on formation rates is discussed using reaction path diagrams.

#### Formation trends at different locations of the flame

Depending on the flame location different  $NO_x$  formation mechanisms occur.

Figure 4.16 shows instantaneous reaction rates at different reaction progress points. Hence, one can observe the significance of  $NO_x$  formation paths at different flame positions.

The discretization point of 25% temperature progress is located shortly before the flame front. The reaction path diagram in 4.16a shows only a few species. Reactive NO molecules favor the formation of  $NO_2$ . Additionally, reactive compounds like NH, HNO or  $NH_2$  react to more stable configurations.

At 50% temperature progress many intermediate species appear in the reaction path diagram. The Fenimore mechanism of  $NO_x$  formation deals with CH and  $CH_2$  radicals that are reacting together with  $N_2$  to HCN and NH. In preceding chain reactions these species subsequently form Nitric Oxide (NO). The reaction path diagram shows many paths involving these intermediate species. Hence, it becomes clear that this pathway needs to be considered at test conditions. In the flame front the Fenimore mechanism is dominant.

Furthermore, species involved in the *NNH* mechanism are observed in the flame front. As described in section 2.2.3 these species are decomposed to *NO* afterwards. A slight influence of this mechanism is evident in the reaction path diagram 4.16b.

Spatially less than 1mm downstream is the location corresponding to 75% temperature progress. This zone appears to have a strong influence on  $NO_x$  formation as the scaling factor of the diagram is at a maximum. This reveals that many reactions occur very fast at this location.

In detail, the prompt mechanism and the NNH mechanism play a major role at this location; hydrocyanic acid (HCN) and NNH are decomposed to Nitric oxide NO. Additionally, the thermal path of  $NO_x$  formation appears in the reaction path diagram 4.16c. The thermal path requires bigger time scales and thus, reaction rates are usually quite low. Peak atomic oxygen concentrations occur in the flame front which are called super-equilibrium conditions. Hence, also the thermal path's reaction rates are increased and appear in the diagram with low coefficients.

Even though the adiabatic temperature is reached not all chemical reactions have attained an equilibrium state. At this location the thermal path of  $NO_x$  formation is predominant. In the reaction path diagram this is evident by the arrows connecting the species  $N_2$ , N and NO. Because of relatively long residence times in the combustion chamber, the Zel'dovich mechanism contributes most to NO formation. Furthermore, the  $N_2O$  depletion reaction forms NO

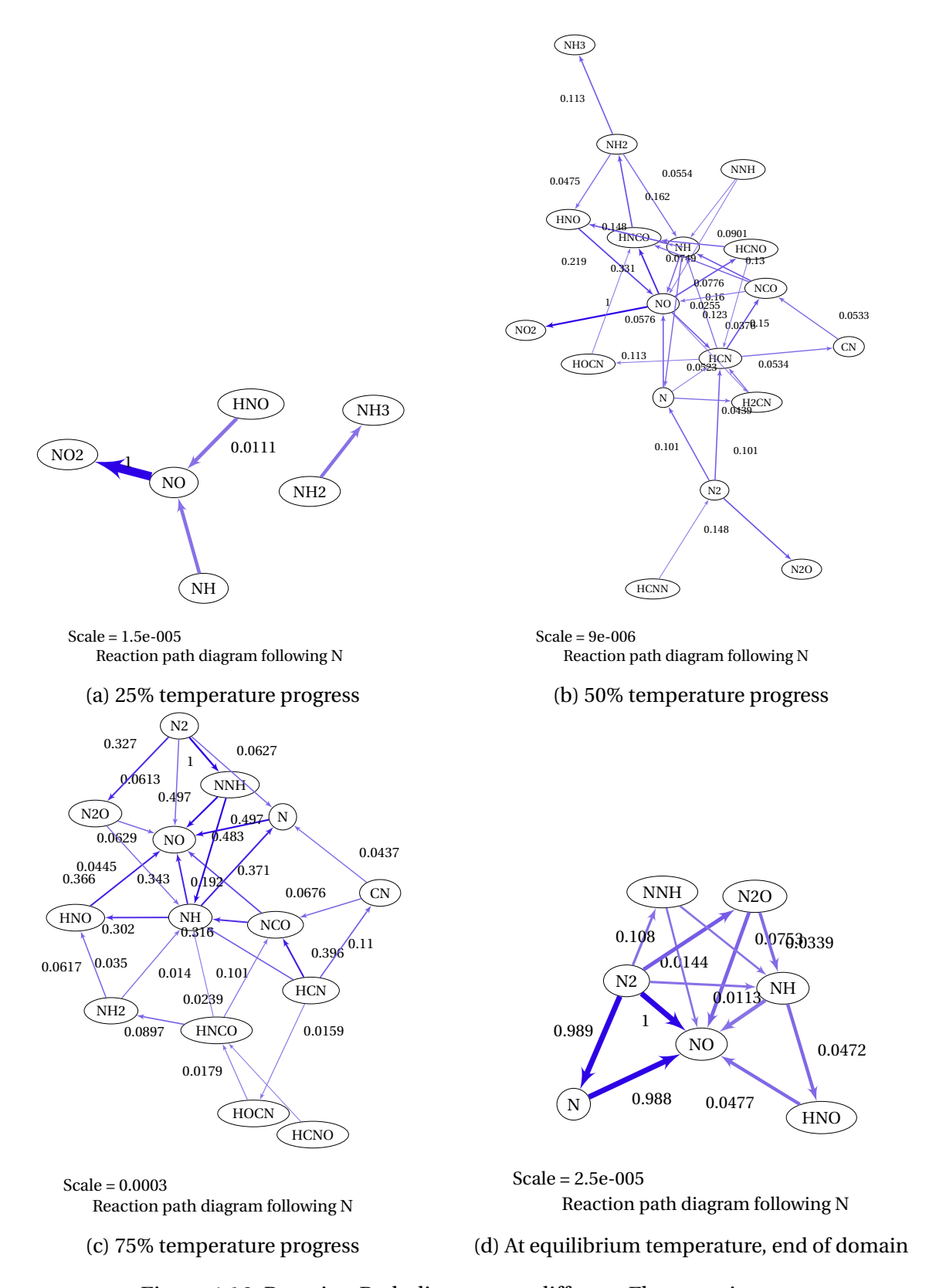


Figure 4.16: Reaction Path diagrams at different Flame regions

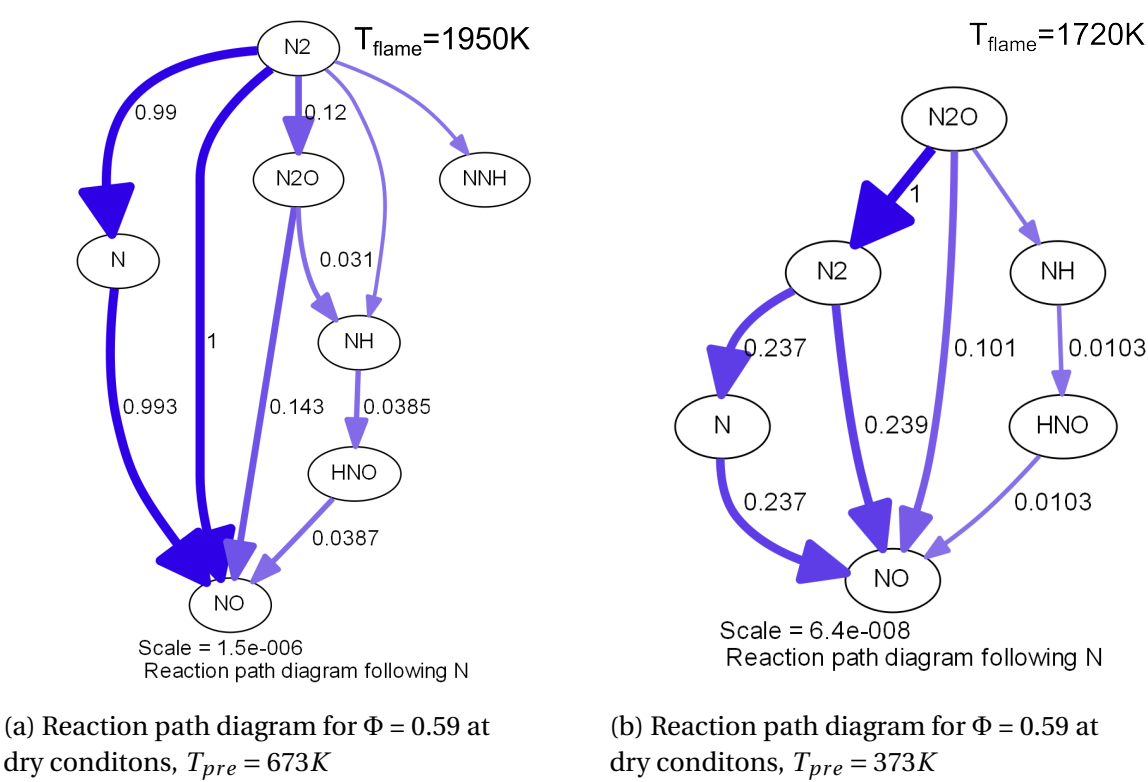
downstream of the flame front.

In conclusion, due to low temperatures  $NO_x$  formation rates prior to the flame front are negligible. In the flame front intermediate species are present. Hence, the prompt and NNH mechanism are in particular responsible for  $NO_x$  formation in the flame front. Subsequently in the post-flame zone the thermal path of  $NO_x$  production is predominant. Also, the  $N_2O$ depletion reaction contributes to post-flame zone  $NO_x$  formation.

Phenomena of water injections are studied in the following regarding the  $NO_x$  formation in the post-flame zone.

#### Influence of temperature on reaction paths

The temperature dependence of reaction paths in the post-flame zone is analyzed in the following. Varying preheat temperatures result in different flame temperatures. Therefore, the temperature dependence of reaction pathways becomes evident when comparing reaction path diagrams for different inlet temperatures.



dry conditions,  $T_{pre} = 673K$ 

Figure 4.17: Reaction Path diagrams for different preheat temperatures

Reaction path diagrams for different preheat temperatures are plotted in figure 4.17. A sample fuel-to-air ratio  $\Phi$  is chosen since major changes are clearly visible.

In the case of  $T_{pre} = 673K$  the reaction of atmospheric nitrogen  $N_2$  to NO is referenced by one. Besides, the decomposition of  $N_2$  to N which further forms NO is approximately one. These two reactions are exactly the thermal pathway of  $NO_x$  formation. Nitrous oxide depletion contributes to NO emissions with a factor of 0.143, significantly less than the thermal path. Hence, one can conclude that the thermal pathway is dominant in the  $NO_x$  formation rate. At this test conditions a flame of ~ 1950K is reached.

At a preheat value of 373K and an equivalence ratio of  $\Phi=0.59$  one attains an adiabatic flame temperature of 1720K. This decrease in flame temperature leads to different formation paths. One can observe that the Nitrous Oxide depletion to  $N_2$  is the most significant reaction involving Nitrogen. Still, the thermal path of  $NO_x$  formation can be distinguished well in the diagram. Values of about 0.24 are indicated for formation reaction rates. The second most important contributor for NO formation is the depletion of  $N_2O$  to NO. The influence of this  $N_2O$  reaction path rises as  $T_{pre}$  decreases due to the decline in Zel'dovich production rates. Looking at the scale one is reminded of the observed decay in  $NO_x$  formation for lower preheat temperatures.

#### Reaction path changes by water injection in the flame front

In the following section the impact of water injection on reaction paths is studied. As expected  $NO_x$  formation rates are reduced for declines in flame temperature. A temperature drop similar to lower preheat values occurs for water injections. However, a setup of constant flame temperatures is more interesting. Formation rate discrepancies are in this setup only influenced by changes in the combustion chemistry for added water.

Hence, reaction path diagrams in the flame front for two different cases are depicted at constant flame temperature. The corresponding point is located where the mixture has reached 50% temperature progress ( $\frac{T-T_{in}}{T_{end}-T_{in}}=0.50$ ). Figure 4.18a shows the reaction paths at no water injection, figure 4.18b corresponds to a water injection  $\Omega=1.0$ .

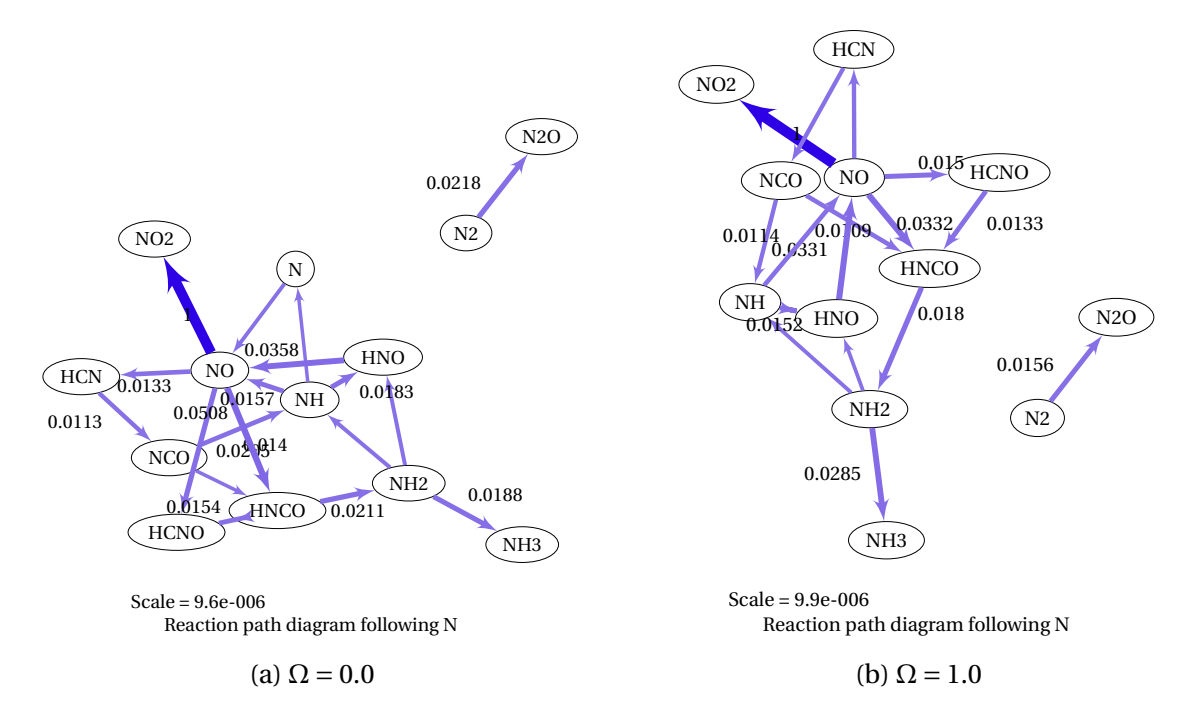


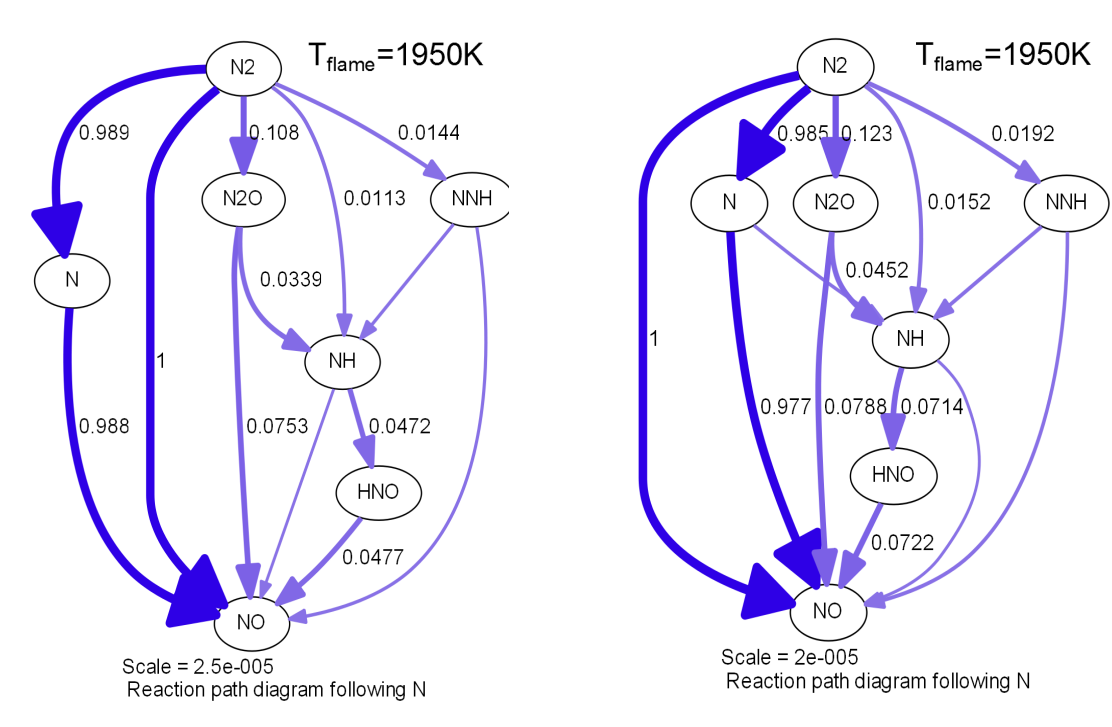
Figure 4.18: Reaction paths at 50% temperature progress at constant flame temperature,  $T_{pre} = 573K, \Phi = 0.625$ 

One is reminded that the same flame temperature occurs in both cases. As a result only minor changes in the reaction paths are observed. The relative scale of the diagrams is slightly bigger in the wet scenario. In both cases the reaction of NO to  $NO_2$  is the strongest. Because of the scale this means that in the wet cases absolute formation rates of NO to  $NO_2$  is slightly higher. Furthermore changes in the decomposition of NO to other species are computed.

In conclusion, the changes in the flame front are very slight and hardly evident. Nevertheless, the wet scenario produces less  $NO_x$  emission concentrations. A particular reason for that change is not found in the reaction paths within the flame front.

#### Reaction path changes by water injection in the post-flame zone

In the following the changes in the post-flame zone are considered. Therefore, in figure 4.19 reaction path diagrams are depicted for rising water injection rates  $\Omega$ . In this setup the temperature is held constant at  $\sim 1950K$ ; hence differences are solely influenced by changes in radical concentrations.



(a) Reaction path diagram for  $\Phi$  = 0.71 at dry conditions

(b) Reaction path diagram for  $\Phi$  = 0.79 at  $\Omega$  = 1.0

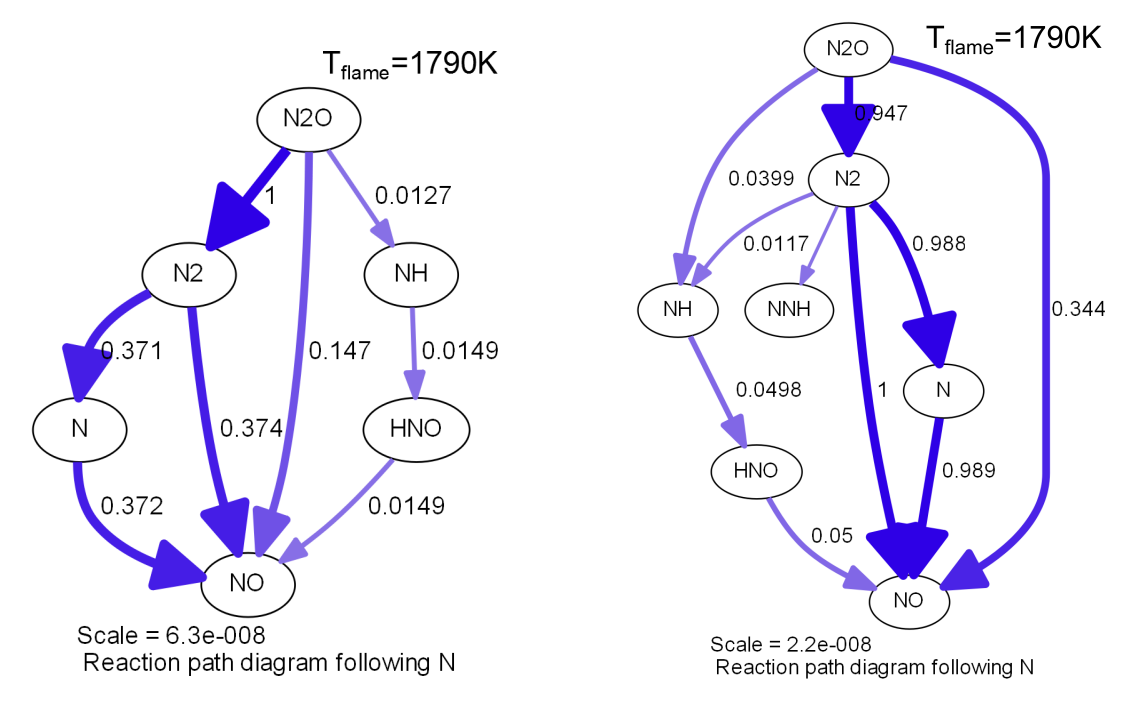
Figure 4.19: Reaction Path diagrams of the post-flame zone for increasing water injections at constant flame temperature,  $T_{pre} = 673$ ,  $\Phi = 0.71$ 

One can observe that the physical effect of the temperature drop generally influences  $NO_x$  formation more significant than radical changes due to present water. The values and scales vary only slightly in the figure 4.19.

 $NO_x$  formation mechanisms at this regime (near stoichiometric and high  $T_{pre}$ ) are mainly driven by the Zel'dovich pathway due to high flame temperatures. Comparing the two dia-

grams in figure 4.19 no great differences in the relative formation paths are calculated. However, by looking at the diagram scales one can conclude that e.g. the thermal path is indeed influenced although temperatures remain constant. The reason for these influences are decreasing atomic oxygen concentrations as more water is injected. As a consequence the rate limiting reaction of the thermal path is hindered and lower absolute  $NO_x$  formation rates are observed.

Additionally, the water influence on reaction paths is described for lower flame temperatures. For  $\Phi=0.56$  and  $T_{pre}=473K$  adiabatic flame temperatures of approximately 1790 K are reached.



- (a) Reaction path diagram for  $\Phi$  = 0.56 at dry conditions
- (b) Reaction path diagram for  $\Phi$  = 0.598 at  $\Omega$  = 1.0

Figure 4.20: Reaction Path diagrams for increasing water injections - setup of constant temperatures,  $T_{pre} = 473$ ,

At this regime a greater difference between the dry configuration and  $\Omega=1.0$  occurs. However, changes in the formation rates relevant for  $NO_x$  emissions, are similar to the previous case,  $\Phi=0.71$  and  $T_{pre}=673K$ .

The Zel'dovich path of NO formation is slightly affected, comparable to the previous case. Multiplying the values with the scaling one obtains the absolute formation rates. The absolute decrease is similar to the decline in oxygen radical concentrations.

Especially, significant differences in the  $N_2O$  depletion reaction become evident. Hence, the reaction from  $N_2O$  to NO produces an roughly equal amount of NO in both configurations. However, the depletion of  $N_2O$  to atmospheric  $N_2$  becomes less likely with higher water proportions. Although smaller  $N_2O$  concentrations occur in wet configurations they relatively contribute more significantly to NO.

## 4.5 Comparison of Numerical Results with Experimental Data

The simulation tool is designed to model the residence time distribution of the experimental test rig. The main task of the numerical simulation is to calculate experimentally measured  $NO_x$  concentrations. Therefore, a comparison between physical and numerical results is important for verification.

In a first step the experimental data is presented. In a second step the numerical data is fitted to experiments with a corresponding heat transfer coefficient.

#### 4.5.1 Experimental Results

Experimental emission results are obtained in the test rig in the course of a PhD thesis [14] by the supervisor of this thesis. An experimental study is vital in order to investigate the feasibility of water injection in the combustion chamber.

#### **Constant Equilibrium ratio**

Figure 4.21 shows relative  $NO_x$  emission trends corresponding to the dry configuration. The experimental measurements are depicted next to numerical results.

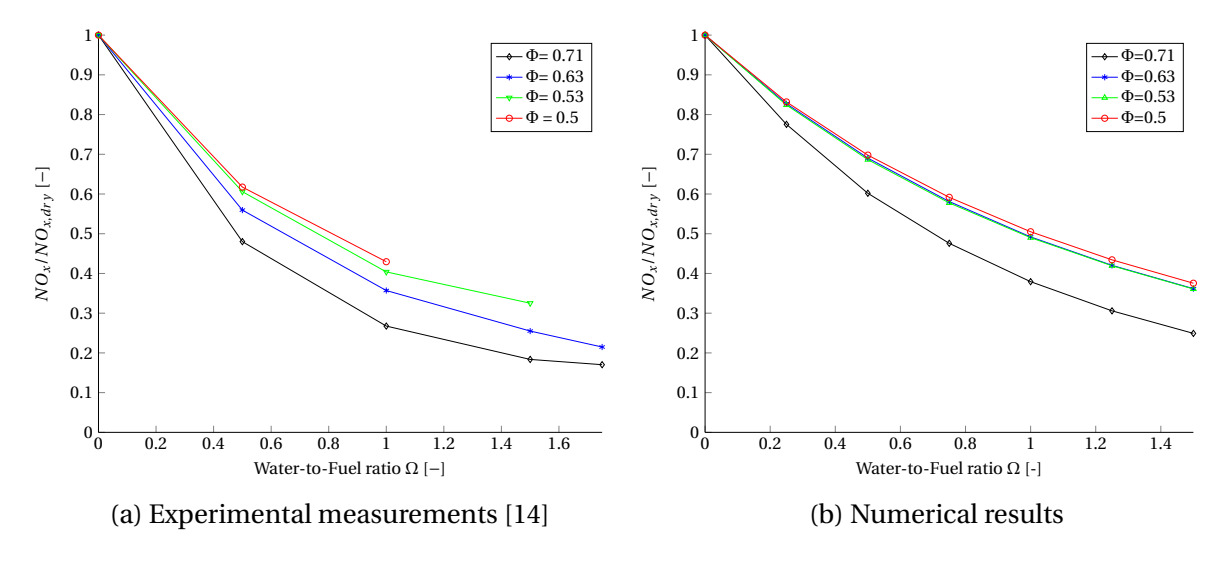


Figure 4.21: Comparison of experimental and numerical  $NO_x$  emission values at constant equivalence ratio  $\Phi$ 

The relative trends of experimental  $NO_x$  emission values correlate well to numerical calculations in the scenario of constant equilibrium ratios  $\Phi$ . The experiment uses liquid water, whereas the simulation uses steam. Thus, flame temperatures in the experiment decrease stronger than in the numerical simulation setup. As a consequence even a more severe decline of  $NO_x$  values is measured in the experiment than calculated by the numerical tool.

#### **Constant flame temperature**

The setup of constant flame temperatures is also measured in the experimental test rig. Results are plotted in figure 4.22 side-by-side with numerical calculation data.

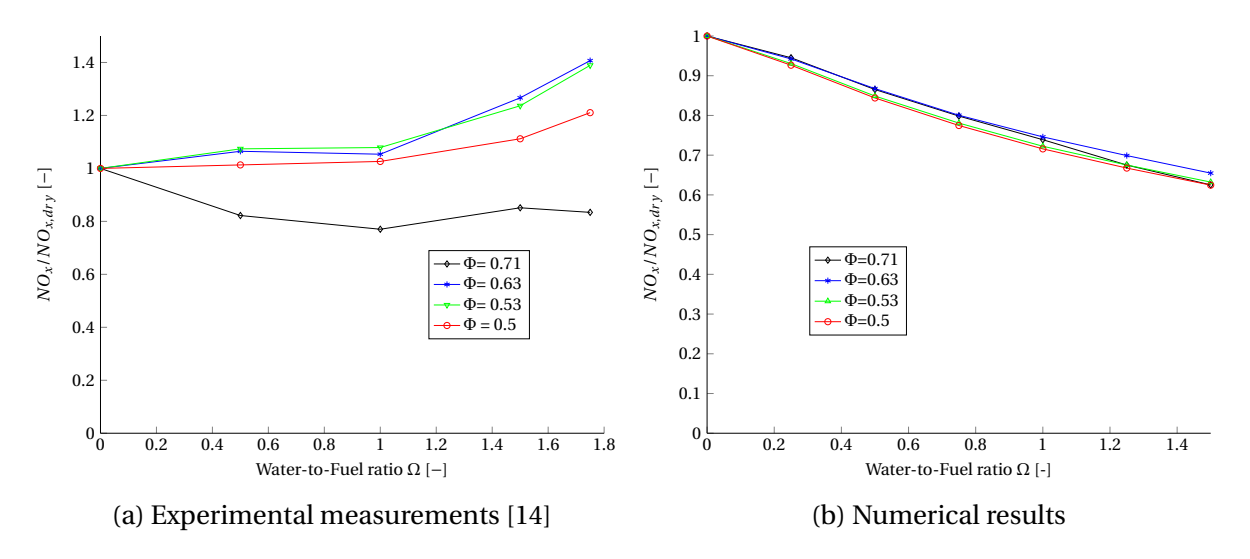


Figure 4.22: Comparison of experimental and numerical  $NO_x$  emission values at constant flame temperature  $T_{flame}$ 

The plots clearly indicate that numerical and experimental results differ significantly. Only the measurement series of  $\Phi=0.71$  and a small water injection ratio shows similar results to the numerical calculations. At lean conditions the experimental profiles rise for higher water proportions. In particular at high water injection ratios  $NO_x$  values strongly rise. Several phenomena are responsible for the observed trends.

Firstly, the experimental and the simulation use different equivalence ratios. In the experiment additional energy is required for the water vaporization. Thus, fuel-richer conditions occur in the experiment which can lead to partially rising  $NO_x$  emissions.

Secondly, in reality the injected water is not perfectly mixed with the air-fuel mixture. Regions can exist where water appears undiluted as droplets. On the contrary also areas with only small amounts of water occur. Such regimes may lead to temperature peaks and thus, to a considerably increased  $NO_x$  formation rate. This effect becomes more important with high water injection rates.

Since a strong rise in  $NO_x$  formation occurs at lean conditions and high  $\Omega$  flame instabilities may also be responsible. These phenomena are not described by the simulation tool. Hence, differences between the simulation and reality occur.

#### 4.5.2 Numerical adjustment with corresponding heat transfer

The numerical simulation constantly over-predicts  $NO_x$  formation due to an adiabatic setup. In reality heat losses to the environment occur. As a result physical temperatures are generally lower than temperatures that are calculated by the simulation. Consequently,  $NO_x$  formation rates in the simulations are over-predicted.

In this section heat loss in the combustion chamber is taken into account. It is difficult to incorporate a heat transfer in the One-dimensional Free Flame calculations. Hence, only heat removal in the post-flame zone is considered. In the reactor network a heat transfer coefficient can be specified. This coefficient was determined in order that the dry  $NO_x$  emission calculations reach the dry experimentally measured values. Hereby, the reactor network is iteratively computed with manually adjusted heat transfer coefficients. The iteration is stopped when differences between experiment and numerical model are negligible small.

In this section results are presented with a heat transfer coefficient corresponding to experiments. This is only calculated for the constant equilibrium case since relative trends are similar. Subsequently, unphysical side effects are evaluated.

#### **Results**

The simulation error becomes particularly important at high adiabatic flame temperatures, i.e. in rising equivalence ratios and high preheated configurations. Hence, results for  $T_{pre} = 673K$  are depicted in figure 4.23.

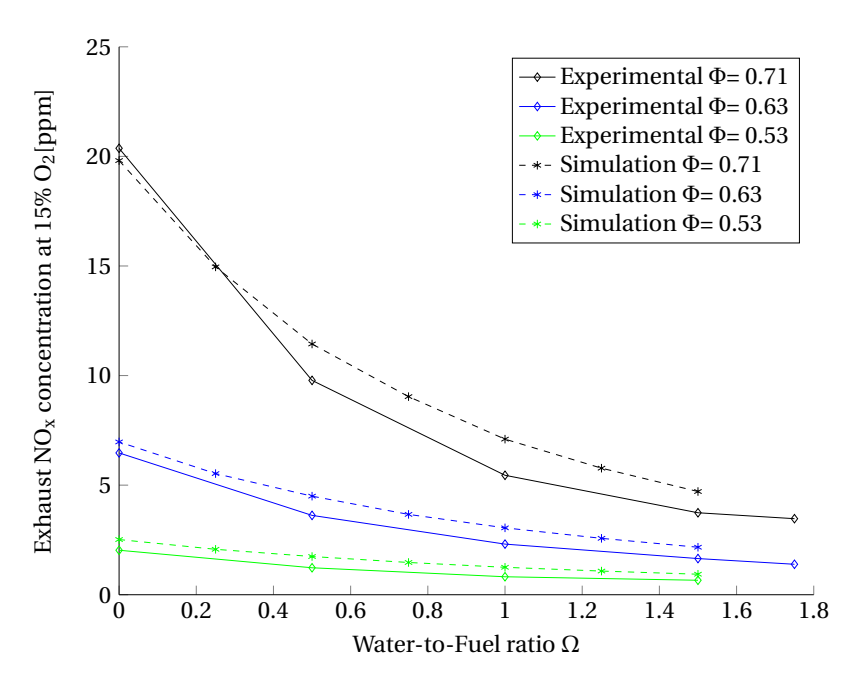


Figure 4.23: Comparison absolute  $NO_x$  emissions between experiment and simulation including heat loss,  $T_{pre} = 673$ 

One can observe that adjusted numerical dry emission concentrations correlate closely with measured values. Nevertheless, the  $NO_x$  decline with rising  $\Omega$  is greater in the experimental setup. As described above, this is due to the fact that liquid water is used in the experimental test rig. The necessity of vaporizing the water cools the experimental flame further down compared to the numerical calculations. To improve this behavior a model for the vaporization cooling needs to be incorporated.

#### Limitations of the correction approach

However, one must keep in mind that this setup does not model all physical phenomena sufficiently. The correction of  $NO_x$  emission values solely takes place in the post-flame zone (PFZ). In reality, heat transfer takes place in the whole burner. Hence, also the flame front is cooled.

Therefore, the  $NO_x$  formation rate in the numerical Free Flame is increased compared to reality. In order for the calculations to correlate to the experiment, an under-prediction in the post-flame zone  $NO_x$  is necessary. The reaction path diagrams in section 4.4.2 show that the Zel'dovich path is predominate in the PFZ. Thus,  $NO_x$  formation rates are strongly dependent on temperature.

A lower temperature in the PFZ results in smaller PFZ  $NO_x$  formation rates. The tool therefore underestimates the exhaust temperature by an unphysical high heat transfer coefficient in a way that  $NO_x$  values at the probe location correspond to the experiment. In the presented results this even leads to an unphysical exhaust temperature of only 600K. Obviously the model differs severely from realistic phenomena. To prevent this side effect  $NO_x$  formation in the flame front needs also to be reduced. Therefore, an incorporation of heat transfer in the Free Flame calculations is necessary. Peak temperatures in the flame front need to be dampened in a way that only a smaller error correction in the PFZ is necessary.

In conclusion, the correction approach calculates results in good agreement for small water injection ratios. For an improvement to higher water proportions a model for the experimental cooling by liquid water vaporization is essential.

For the setup of constant flame temperature further it is necessary to further investigate the phenomena. On the one hand, the experimental results can be imprecise because of local unmixed water in the fuel-air mixture. On the other hand, the numerical calculations may assume unjustified simplifications. This could include the gaseous water assumption or a perfectly mixed solution.

## 5 Conclusion and Outlook

In conclusion, water injection in the combustion chamber has a beneficiary effect on  $NO_x$  formation.

For the first investigated scenario the equivalence ratio is held constant for the water injection. As expected, numerical results show that the adiabatic flame temperature declines. Lower temperatures generally reduce  $NO_x$  formation. This phenomenon is also observed in the numerical model for all investigated measurement points. At near stoichiometric configurations ( $\Phi=0.71$ ) and with a preheat temperature of 673K the  $NO_x$  emission is decreased up to 75% compared to dry combustion. Relative behavior is in good agreement with experimental data.

In a second setup the equivalence ratio was modified in order to keep the flame temperature constant. Even with constant combustion temperatures a considerable decline in  $NO_x$  emission concentrations is calculated. Naturally the  $NO_x$  reduction factor is smaller compared to the previous setup, but still, up to 35%  $NO_x$  can be avoided. These effects are due to different radical concentrations in the combustion process.

A developed reactor network predicts absolute  $NO_x$  concentrations at the probe location. However, the simulation tool constantly over-predicts temperature and  $NO_x$  concentrations. This is due to fact that calculations are performed in an adiabatic manner. In reality, heat loss to the environment occurs which lowers the experimental flame temperature. For a better accuracy of the tool the over-prediction in flame temperature needs to be corrected. Improvements can be made regarding the following simplifications.

In a first step the amount of the heat removal from the combustion chamber needs to be estimated. This involves the radiative heat transfer as well as heat loss by forced convection. In a second step the vaporization process prior to combustion needs to be examined. By disregarding the cooling of the mixture through water vaporization the temperature before the ignited flame is currently also over-predicted. Hence, the determination of the inlet temperature requires a more detailed treatment.

Furthermore, the tool deals with perfectly diluted, gaseous steam. This simplification is necessary in the course of kinetic modeling with Cantera. Local regions of unmixed species contribute to  $NO_x$  formation in the experiment. Additionally, a negative side effect of water injection in gas turbine combustion chamber could be the rise in flame instabilities. One should also keep in mind that the developed model lacks in predicting these phenomena. An experimental study is therefore vital for the investigation of the impact of water injection in gas turbine combustion chamber.

# A Normalization of Emission Concentrations

A normalization of emission data is essential for a comparison to different measurements. It is common to use a 15% Oxygen concentration in the exhaust gas as reference point.

For the normalization procedure the following formula was used:

$$\gamma_{i,15\%O_2} = \gamma_i * \frac{\gamma_{O_2,env} - \gamma_{O_2,norm}}{\gamma_{O_2,env} - \gamma_{O_2,exhaust}}$$

where notations specified in the following table A.1 are used. A derivation of the formula can be found in Turns [22].

Table A.1: Explanation of variables for normalization procedure

$\gamma_{i,15\%O_2}$	Molar concentration fraction of species i, normalized to 15% Exhaust oxygen	
$\gamma_i$	Calculated molar concentration fraction of species i	
$\gamma_{O_2,env}$	Ambient Oxygen concentration fraction, 20.942%	
$\gamma_{O_2,exhaust}$	Exhaust oxygen concentration fraction	
$\gamma_{O_2,norm}$	Reference oxygen concentration, here: 15%	

## **B** Methodology steps

In the following chapter the calculation steps of the simulation are described. Different features of the calculations and the modeling procedure are explained.

#### **B.1** Free Flame simulations

Free Flame calculations are implemented in a *Python* script using the *Cantera* package. For the two different scenarios two *Python* scripts are implemented:

- FreeFlame-ConstantEquivalenceRatio.py
- FreeFlame-ConstantFlameTemperature.py

#### **B.1.1** Constant Equivalence Ratio

This *Python* script calculates One-dimensional Free Flames for constant equivalence ratios. The initial temperature is varied for cases 673K, 573K, 473K, 373K. The calculations use inverse equivalence ratios from 1.4 to 2.0 in steps of 0.1. Water injection rates up to  $\Omega = 1.5$  are calculated.

In the beginning the overall simulation parameters are defined. Then, a for-loop varies the parameters for calculating the different measurement points. The calculation of the Free Flame involves 3 basic steps:

- an initial guess
- an iterative refinement and iteration to reduce temperature/energy residuals
- an iteration including multi-species diffusion processes

The intermediate solution is saved in an .xml file during calculation. When the residuals are within a specified limit the calculation is stopped. The final solution is saved in a .csv file in the same folder. In this .csv file the calculated variables are saved: distance, temperature, velocity, specific volume, temperature, temperature progress and species concentrations.

At last also an instantaneous reaction path diagram is generated at the last grid point of the Free Flame domain.

#### **B.1.2** Constant Flame Temperature

This *Python* script calculates One-dimensional Free Flames for constant flame temperatures. The initial temperature is varied for cases 673K, 573K, 473K, 373K. Water injection rates up to  $\Omega = 1.5$  are calculated. The calculations use dry inverse equivalence ratios from 1.4 to 2.0 in steps of 0.1. In wet cases the equivalence ratio is adjusted to reach the dry flame temperature.

At first, a matrix of equivalence ratios is calculated for specified inlet temperatures. A forloop repeats the following procedure then for all different preheat temperatures.

The mixture is initialized first for dry conditions and corresponding  $\Phi$ . The adiabatic flame temperature is calculated. Subsequently, the water injection is increased. To reach the dry flame temperature the dry inverse equivalence ratio is reduced so that the combustion reaches the same flame temperature.

These equivalence ratios are then used to calculate Free Flames similar to the above mentioned procedure.

Again, .csv files are generated for all measurement points. Be aware that these calculations consume much time on a regular PC. To employ several cores of the PC the python script was run in different consoles as described in chapter 3.

## **B.2** Probability density distribution of residence times

Information about the particle residence time distribution in the combustion chamber is incorporated in the reactor network. This section describes the procedure for calculating the particle residence time. It uses existing CFD calculations on ANSYS CFX. A .csv file of residence times was exported. Subsequently the partitioning and post-processing of the data was computed in Matlab.

## **B.2.1** Calculation of particle residence times in ANSYS

#### Particle injection in the flow domain

The particle injection was performed by using a Particle Injection Region. Many options can be specified. The injection plane was chosen to be at the inlet of the burner. The options are summarized in table B.1.

Option	Value
Injection Method	Full cone
Injection direction	Y-direction (axial)
Velocity magnitude	1m/s

Table B.1: Setting of the particle injection region

Furthermore the particles need material was specified as solid aluminum with a small density. The basic idea is that the particles follow the flow field. A summary of particle settings are depicted in table B.2.

Table B.2: Settings of injected particles

Option	Value
Morphology	Particle transport solid
Particle diameter distribution	Specified diameter of 1e-3 mm
Density	$1.185 \text{ kg } m^3/\text{s (air density)}$

The computations are initialized with the converged solution without particles. Therefore, the calculations demand only few computational effort.

#### Generating residence time data

The following settings have to be specified in *CFX Post*. An isosurface is created setting the axial velocity v to 27 m/s. To select only the regions in the combustion chamber the function 'Iso Clip' is used. Hence only the surface with axial coordinate Y >= 0.135[m] is considered. Particle tracks are created. One can see that they cross the created flame surface well distributed. However, no possibility of measuring the particle time from crossing the isosurface to the domain end was found.

Hence, a reasonable amount of 1000 streamlines are seeded on the Isosurface. The streamlines show similar trajectories to the particles. A chart was created with residence times beginning from the surface to the outlet. The graph plots the streamline number and the time. It shows a well distributed behavior (see figure 3.6). Subsequently, the exporting function was used creating a .csv file of residence times. In the .csv the time for all discretized points of the streamline is saved. The maximum time corresponds to the outlet.

## **B.2.2** Generating a PDF of residence times in MATLAB

To partition the data *Matlab* is used. The created .csv file needs to be manually imported. Subsequently the code GeneratingHistogramAndPDF.m post-processes the data.

First, the *Matlab* code selects only the maximum time of the trajectories since this corresponds to the outlet. Secondly, it corrects unphysical values such as extremely high or low residence times. Thirdly, it creates from the cleaned vector a histogram as displayed in figure 3.6. The sector data is then used in the python script for a weighted average of  $NO_x$  values.

#### **B.3** Reactor Network

For the reactor network another *Python* script is implemented. It uses Free Flame Data at 95% temperature progress. Therefore, first a file of the Free Flame Data is created. Then this file is imported in *Python* and a reactor network applied.

#### B.3.1 Storage of Free Flame data at corresponding location

This section explains how the files from section 3.3.4 in table 3.3 are created.

In the results of the Free Flame additionally a temperature progress variable is saved for each grid point. For each measurement point the species compositions closest to 95% is manually selected. These values are then copied to other files that are called Species.csv and TestConditions.csv. The species file contains the 53 comma separated values of the species at 95% temperature progress. The test conditions file contains  $T_{pre}$ ,  $\Omega$ ,  $\lambda = 1/\Phi$  and  $T_{95\%}$ .

For each preheat temperature one set of these files is created. These files have to be saved in the same folder as the *Python* script. The *Python* script imports these files for reactor initialization and file names.

#### **B.3.2** Reactor network calculations

The implemented Python script is called ReactorNetwork.py. A copy of this file is additionally saved in the same folder as the emission data because of importing data.

First, the upper mentioned files are imported. These files contain the data of a measurement series for a certain preheat temperature. Also, the cases of constant equivalence ratio and constant flame temperature are treated separately.

Secondly, the reactor network is applied. For each test case the parameters are specified. Then a flexible wall is defined so that the pressure remains constant. Initially the reactor is set to the Free Flame 95% values. Then the reactor network advances in time steps of  $10^{-5}$ .

Thirdly, the residence time data is taken into account. A weighted average of the residence times need to be calculated. For each residence time sector the corresponding approximate time step in the reactor is selected. All sector concentrations are summed up weighted to the histogram height. As a result one obtains a weighted average of concentration data. This average corresponds to particle residence times at the experimental emission probe location.

In a last step these emission concentrations of the whole measurement series is saved in a .csv file.

## **B.4** Postprocessing of calculations

## **B.4.1** Reaction Path diagrams

Reaction path diagrams are generated in the upper mentioned Free Flame calculations. These diagrams display instantaneous reaction paths at the last grid point in the Free Flame domain. This section explains a procedure to create reaction path diagrams at arbitrary flame locations. Therefore, the *Python* script CreateReactionPathDiagramForDesiredPoint.py was implemented.

One needs to specify the species composition and temperature of the desired configuration. The *Python* script initializes a PSR with constant pressure. Only one very small time step of  $10^{-5}$  s is applied. Then a reaction path diagram is generated as a .dot and .png file.

#### **B.4.2** Creating Plots of calculated data

#### **Free Flames**

In the directory of the Free Flame data also a *Matlab* file Temperature\_Plot.m is saved. These files import the Free Flame Data of the folder. It creates different plots and few of them are depicted in this thesis. By having all the data imported in *Matlab* it is easy to compute other desired graphs.

#### **Reactor Network**

For visualizing the reactor network data a Matlab file PlotReactorNetworkEmissionData.m is written. Therefore, first one needs to manually import the .csv file of weighted averages produced by the reactor network script. It includes a whole measurement series for a certain preheat temperature. Then it creates several plots of the emission data. Relative as well as absolute  $NO_x$  exhaust concentrations are plotted.

# **Bibliography**

- [1] Inc. ANSYS. ANSYS Academic Research, Release 14.0, 2011.
- [2] Craig T Bowman. Investigation of Nitric Oxide Formation Kinetics in Combustion Processes: the Hydrogen-oxygen-nitrogen Reaction. *Combustion Science and Technology*, 3(1):37–45, 1971.
- [3] Joseph W Bozzelli and Anthony M Dean. O+ NNH: A possible New Route for NOx formation in Flames. *International Journal of Chemical Kinetics*, 27(11):1097–1109, 1995.
- [4] Sanjay M Correa. A Review of NOx Formation under Gas-turbine Combustion Conditions. *Combustion Science and Technology*, 87, 1993.
- [5] Gregory P. Smith et al. GRI-Mech 3.0. http://www.me.berkely.edu/gri\_mech/, 05/2014.
- [6] M Falcitelli and S et al. Pasini. CFD+ Reactor Network Network Analysis: An Integrated Methodology for the Modeling and Optimisation of Industrial Systems for Energy Saving Pollution Reduction. Applied thermal engineering, 22(8):971–979, 2002.
- [7] Vincent Fichet, Mohamed Kanniche, Pierre Plion, and Olivier Gicquel. A reactor network model for predicting NOx emissions in gas turbines. *Fuel*, 89(9):2202–2210, 2010.
- [8] David G. Goodwin, Harry K. Moffat, and Raymond L. Speth. Cantera: An Object-oriented Software Toolkit for Chemical Kinetics, Thermodynamics, and Transport Processes. http://www.cantera.org, 2014. Version 2.1.2.
- [9] SC Hill and L Douglas Smoot. Modeling of Nitrogen Oxides Formation and Destruction in Combustion Systems. *Progress in energy and combustion science*, 26(4):417–458, 2000.
- [10] Christof Lechner. Stationäre Gasturbinen. Springer DE, 2009.
- [11] C Mayer, J Sangl, and T et al. Sattelmayer. Study on the Operational Window of a Swirl Stabilized Syngas Burner Under Atmospheric and High Pressure Conditions. *Journal of Engineering for Gas Turbines and Power*, 134(3), 2011.
- [12] Christoph Mayer. Konzept zur vorgemischten Verbrennung wasserstoffhaltiger Brennstoffe in Gasturbinen. PhD thesis, Technische Universität München, 2012.
- [13] Klaus Georg Moesl. *On the Formation of Nitrogen Oxides During the Combustion of Partially Pre-Vaporized Droplets.* PhD thesis, Technical University of Munich, 2012.

- [14] Stephan Lellek M.Sc. Personal communication and distribution. Lehrstuhl für Termodynamik, Technische Universität München, 2014.
- [15] Judith Kathrin Paehr. Reduction of Quenching by Increasing Turbulence in Gas Turbine Combustion Systems to Reduce CO Emissions at Part Load. Diploma Thesis, RWTH Aachen University, 2010.
- [16] Thierry Poinsot and Denis et al. Veynante. *Theoretical and Numerical Combustion*. R.T.Edwards, 2005.
- [17] A Richters and K Kuratis. Air pollutants and the Facilitation of Cancer Metastasis. *Environmental health perspectives*, 52:165, 1983.
- [18] J Sangl, C Mayer, and T Sattelmayer. Dynamic Adaptation of Aerodynamic Flame Stabilization of a Premix Swirl Burner to Fuel Reactivity Using Fuel Momentum. *Journal of Engineering for Gas Turbines and Power*, 133(7):071501, 2011.
- [19] Janine Sangl. Erhöhung der Brennstoffflexibilität von Vormischbrennern durch Beeinflussung der Wirbeldynamik. PhD thesis, Technische Universität München, 2011.
- [20] Thomas Sattelmayer. Thermodynamik 2. *Lehrstuhl für Thermodynamik, Technical University of Munich*, 2008.
- [21] SWM Services GmbH. Erdgasqualität Im Verteilungsnetz des Großraumes München, 2014.
- [22] Stephen R Turns et al. *An Introduction To Combustion*, volume 287. McGraw-Hill New York, 1996.
- [23] G.Cornelis van Kooten. Wind Power: The Economic Impact of Intermittency. *Letters in Spatial and Resource Sciences*, 3(1):1–17, 2010.
- [24] Jürgen Warnatz, Ulrich Maas, and Robert W Dibble. *Combustion: Physical and Chemical Fundamentals, Modeling and Simulation, Experiments, Pollutant Formation.* Springer, 2006.